


NUREG/CR-1509/20f4
SAND80-1304/2of4
R3

LIGHT WATER REACTOR SAFETY RESEARCH PROGRAM
QUARTERLY REPORT, APRIL-JUNE 1980

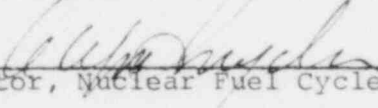
Person in Charge: Marshall Berman

Date Published: August 1980

APPROVED:



Manager, Light Water Reactor Safety Department



Director, Nuclear Fuel Cycle Programs

Sandia National Laboratories
Albuquerque, NM 87185
Operated by
Sandia Corporation
for the
U.S. Department of Energy

Prepared for
Division of Reactor Safety Research
Office of Nuclear Regulatory Research
U.S. Nuclear Regulatory Commission
Washington, D.C. 20555
Under Memorandum of Understanding DOE 40-550-75
NRC FIN Nos. A-1019, -1030, -1227, -1237

8011030495

CONTENTS

	<u>Page</u>
1 Molten Fuel/Concrete Interactions Study	1
1.1 Summary	1
1.2 CORCON Model Development	6
1.3 Acquisition of German Fuel Melt/Structural Materials Interactions Computer Codes	20
1.4 References	27
2 Steam Explosion Phenomena	29
2.1 Summary	30
2.2 Single-Drop Steam Explosion Studies with Molten Iron Oxide	33
2.3 Fully Instrumented Test Series	48
2.4 Modelling and Analysis of Steam Explosions	62
2.5 Structural Consequences of the Steam Explosion	78
2.6 References	78
3 Separate Effects Tests for TRAP Code Development	81
3.1 Introduction	81
3.2 Progress	82
3.3 Fission Product Reaction Facility	84
4 Containment Emergency Sump Performance	87
4.1 Summary	87
4.2 Sump Geometry and Test Variable Definitions	88
4.3 Test Planning	91
4.4 Data Analysis	95
4.5 References	104

ILLUSTRATIONS

<u>Figure</u>		<u>Page</u>
1-1	Concrete Penetration Model	13
1-2	Shear Rate Dependence of Slurry Viscosity	18
2-1	Iridium Wire Weight Loss for Seventeen Experiments	36
2-2	Single frame reproduced from film of iron oxide drop descending in water prior to triggered explosion.	38
2-3	Same conditions as in Figure 2-2, except that drop had fallen 20 mm before entering the water.	39
2-4	Same conditions as in Figures 2-2 and 2-3, except that drop had fallen 15 mm before entering the water.	40
2-5	Photomicrograph of debris collected from spontaneous steam explosion of molten iron oxide drop in water.	43
2-6	Same as Figure 2-5, except that this image shows the corresponding filter paper from which the debris in Figure 2-5 was removed.	44
2-7	Particle diameters of debris shown in Figures 2-5 and 2-6, shown as a function of cumulative weight fractions of the debris.	46
2-8	Particle diameters of debris from triggered explosion of molten iron oxide drop in water, shown as a function of cumulative weight fractions	47
2-9	Sketch of chamber in which laser melted iron oxide drops will be dropped into water at ambient pressures up to 1.0 MPa.	51
2-10	Transient Pressure in FITS Chamber for FITS2A (Pressure Transducer P6)	55
2-11	Transient Pressure in FITS Chamber for FITS2A (Pressure Transducer P7)	56
2-12	Particle Sieve Size Data (FITS1A and FITS2A)	57
2-13	Fuel Debris for Particle Sizes Greater than 500 μm for FITS1A	59

Illustrations (cont'd):

<u>Figure</u>		<u>Page</u>
2-14	Fuel Debris for Particle Sizes Greater than 500 μm for FITS2A	60
2-15	Pressure in Containment, in PT 3 TMLB'	64
2-16	Conceptual Drawing of MARCH Model for Vessel Failure	65
2-17	Various Possible Modes of Lower Plenum Failure	66
2-18	Block Diagram of the Possible Scenarios for Molten Core Entry into the Reactor Cavity	68
2-19	Debris Bed Limiting Steam Pressurization Surry Reactor - TMLB' Accident	70
2-20	One-Dimensional Explosion Calculation Using a Thermal Fuel Fragmentation Mechanism for $\alpha_F = 3.5\%$	75
2-21	One-Dimensional Explosion Calculation Using a Thermal Fuel Fragmentation Mechanism for $\alpha_F = 27\%$	76
3-1	Fission Product Reaction Facility	85
4-1	Details of the ECCS Sump under Investigation in the CESP Program	89
4-2	Screen Blockage Schemes Suggested for Tests	94
4-3	Proposed Nonuniform Approach Flow Tests	96

TABLES

<u>Number</u>		<u>Page</u>
2-I	Experimental Parameters for Interactions Between Single Drops of Molten Iron Oxide and Liquid Water	49
2-II	FITS2A Parameters	53
2-III	Sieve Characteristics	58
2-IV	MD-18 Description	61
2-V	Parametric Study of a One-Dimensional Steam Explosion	73
4-I	Sump Geometric, Flow and Fluid Property Variables	90
4-II	First Twenty-five Test Configurations	93
4-III	Fractional Factorial Design ($1/3 \times 3^4$) for the Factors d, L, B, and b	98
4-IV	Fractional Factorial Design ($1/2 \times 2^5$) for the Factors d, L, B, e_x , and g	99
4-V	Form of Analysis of Variance for Three Level Factors d, L, B, and b	101
4-VI	Form of Analysis of Variance for Two Level Factors d, L, B, e_x , and g	103

LIGHT WATER REACTOR SAFETY RESEARCH PROGRAM
QUARTERLY REPORT, APRIL-JUNE 1980

1. Molten Fuel/Concrete Interactions Study
(T. J. Bartel, R. K. Cole, M. L. Corradini, J. F. Muir, D. A. Powers)

1.1 Summary

The Molten Fuel Concrete Interactions (MFCI) study is comprised of experimental and analytical investigations of the chemical and physical phenomena associated with interactions between molten core materials and concrete. Such interactions are possible during hypothetical fuel melt accidents in light water reactors (LWR's). Our main purpose is to identify and understand the dominant phenomena in order to evaluate the following:

1. The generation rate and nature of evolved noncondensable gases.
2. The effects of gas generation on fission product release.
3. The mechanism, rate, and directional nature of concrete erosion by the melt.

In addressing this objective, the experimental program was divided into four distinct areas:

1. Deposition of Corium-type melts onto concrete.
2. Kinetics and stoichiometry of the thermal decomposition of concrete.
3. Response of concrete to high heat fluxes at one surface.
4. Simulation experiments exploring phenomena at the interface between a melt and a decomposing solid.

The analytical program is directed toward the development of a computer model of molten core material concrete interactions capable of providing quantitative estimates of reactor fuel-melt accident situations. This effort was undertaken in two phases:

1. Development of a preliminary interaction model based on the earliest results from the experimental program - INTER.
2. Development and verification of an improved interaction model that involves a more detailed and refined treatment of the interaction phenomena - CORCON.

CORCON development activities during the quarter encompassed a variety of subjects including numerical and coding changes and improvements, the application of CORCON-MOD0⁺ to the Code Comparison Test Analysis, and

the development of new phenomenological models for future improvements to the code.

Code improvement efforts were devoted primarily toward eliminating problems in the melt/gas-phase chemical equilibrium solution algorithm. A procedure was developed that converges to a true solution for those situations tried to date and, for most of these cases, it does so in a reasonable number of iterations (≤ 25). Other CORCON improvement activities concentrated on clean-up, simplification, and general modifications of the initial version of the code.

The Code Comparison Test Analysis continued using the improved initial version, CORCON-MOD0⁺. Successful runs were made for almost the entire test time (~3000sec). Some minor problems were encountered in making these runs and they were corrected. Preliminary results indicate that the melt temperature falls rapidly to ~1850K during the first ~500s. Power supplied to the melt by the induction coils subsequently reheats the melt to ~1870K, after which it slowly cools in a quasi-steady fashion as the power supplied decreases.

Work continued on the development of a decay heat generation model for inclusion in CORCON. The SANDIA-ORIGEN code was used to obtain decay power and mass

concentrations of the energetic elements for a 20 day period following shutdown. The core condition was conservatively assumed to be that which would yield the maximum expected decay heat generation. The energetic elements have been divided into four groups according to their chemical nature. An aerosol generation model will be included to describe the temporal mass depletion of these groups from the melt.

A simple transient model for the penetration of a hot solid mass (e.g., core debris) into concrete was developed. Energy balance equations for the oxidic and metallic phases relate the temperature change of each phase to the algebraic sum of the energy added to, and lost from, the phase. A two-phase gas-molten concrete (slag) layer formed by the ablation of the concrete is assumed to exist at the core-debris/concrete interface. Initial results from preliminary calculations provide several insights into the phenomena. The most significant is that the heat loss rate from the core debris may be less than the volumetric heat generation rate at early times (on the order of several hours). This implies that the time to stable and final freezing of core debris could be on the order of months as opposed to a few hours as predicted by existing melt concrete interaction codes such as WECHSL and CORCON; i.e., the debris could cycle between liquid and solid states for a long time.

One phenomenon that must be considered in addressing long-term melt/concrete interaction behavior is crust formation and growth during solidification of the oxidic phase of a core melt. The precipitation of solids in siliceous melts will cause the viscosity of the resulting slurry to differ from that of the single phase melt. In general, such slurries are thixotropic, i.e., the viscosity is a non-linear function of shear rate. Furthermore, at zero shear rate, the slurry viscosity is also a non-linear function of the particulate volume fraction. Correlations are presented for the viscosity of slurries which model both of these effects. They show that slurry viscosity increases with particulate volume fraction and with decreasing shear rate.

As part of the USNRC/FRG information exchange agreement in the area of fuel melt research, Mr. Vernon Badham, UCLA, visited Germany during the period May 5-16, 1980, to obtain a number of German computer codes which model various aspects of the interaction of molten core materials with reactor structural materials. Facilities visited included: Kernforschungszentrum, Karlsruhe (KfK); Kraftwerk Union, Erlangen (KWU); and Universität of Hannover (UH). Computer tapes were obtained containing the codes: WECHSL (KfK); KAVERN and BETZ (KWU); and THEKAR (several versions), HEMIS, BETON, BETSI, TEMBET, and SACRI (UH).

Mr. Badham visited Sandia for the week of May 19-23 to transmit the tapes, code input and operation instructions, and all documentation obtained, and to assist in the set-up and check-out of the codes on the Sandia computer. The various programs and data files have been made into permanent files on the CDC system. All programs have been successfully compiled and all but BETSI 3.1 are free of Fortran errors. Sample problem calculations have been made with several of the codes. Brief descriptions, giving the essential features of the programs, are provided in Section 1.3.

1.2 CORCON Model Development

Development of an improved molten core/concrete interaction model, CORCON, continued. CORCON is a user oriented computer program written in a modular structure in which most computational units are contained in separate subroutines. Maximum use is made of existing codes and subroutines. Phenomenological models developed for the code have relied heavily on existing techniques, and data and correlations available in the literature. Numerous input options provide a flexibility that enables a variety of problems to be solved by merely changing input data.

1.2.1 Improvements to CORCON-MOD0

The melt/gas-phase chemical equilibrium solution algorithm was determined to be the main weakness in the code at present. The problem is not so much that the solution technique is seriously inaccurate, but rather that the inaccuracies are random. Consequently, small changes in input variables, such as one would make in a parametric or sensitivity study, lead to random variations in the calculated equilibria. It is impossible to separate these variations from those attributed solely to the changes in the input parameters. An investigation was undertaken to explore the possibility of using an alternate solution technique. It was concluded that none of the alternative methods found was likely to be better than the present one - each has its own problems which differ from, but are not necessarily smaller than, those in the present technique. This being the case, an effort was initiated to try and reduce or eliminate the problems in the existing solution algorithm.

This effort was very successful. A procedure was developed which appears to work satisfactorily. It converges to a true solution for those situations tried to date and, for most of the cases, it does so in a

reasonable number of iterations (≤ 25). It is anticipated, however, that a set of conditions will be encountered in the future where the solution will fail to converge. In the interest of avoiding this situation, an effort to improve the current procedure will continue. However, as long as the solution continues to converge, it is no longer the limiting problem in CORCON. Consequently, the activity devoted to improving the solution procedure will continue at a lower level of effort.

Other CORCON improvement activities concentrated on clean-up, simplification, and general modifications of the initial version of the code. These included:

1. Extensive revamping of the common blocks.
2. Removal of redundant variables.
3. Check-out and incorporation of model changes (such as the new chemical equilibrium solution procedure discussed above) into the code.
4. Addition of a capability to select different levels of printed output by variation of an input parameter. This was done in part to permit suppression of rather extensive diagnostic print messages at the discretion of the user.
5. Improvement of the plotting routines in several ways, including addition of the capability to generate plots independent of whether a calculation terminates normally or abnormally.

1.2.2 Code Comparison Test Analysis

The Code Comparison Test Analysis continued during this quarter. CORCON-MOD0⁺ was successfully run for almost the entire test time (~3000 sec). In performing this analysis, some minor problems were identified in the computer model. For example, the existing decay heat generation subroutine, DHGEN, was modified to accommodate the situation in which either the metallic or the oxidic layer does not has a power input.

Another problem was encountered during the initial cool down of the steel melt before energy was supplied to sustain it above its melting temperature. As the temperature of the steel melt decreased, the code experienced temperature oscillations between 1807 K and 1812 K for a couple of timesteps. This oscillatory behavior corresponds to a temperature (~1809 K) where the iron component of the steel begins to freeze and an enthalpy discontinuity exists due to the latent heat of fusion. A temporary fix in the code structure was employed to alleviate the problem for the code comparison test analysis. This same behavior had been previously noted for INTER, and a more thorough investigation of the problem in CORCON is now underway. Further CORCON calculations will be made following the incorporation of the improved chemical equilibrium solution procedure.

Preliminary results indicate that the melt temperature falls rapidly to ~1850 K during the first 500 seconds. Power supplied to the melt by the induction coils subsequently reheats the melt to ~1870 K, after which it slowly cools as the power supplied decreases.

1.2.3 Decay Heat Generation Model

A dynamic decay heat generation model is being developed for CORCON. The energetic elements, which include not only fission products but irradiated structural material as well, have been divided into four groups according to their chemical nature. The model will include the temporal mass depletion of these groups from the melt. This will be done using an aerosol generation model which considers mass transport by both mechanical sparging and vaporization.

A decay heat model for this application can vary in complexity and degree of sophistication. The current model embodies features which will allow a fairly accurate modeling of the process. These features are:

- total decay heat curve fits determined from a large data base
- core burnup considered in initial mass concentrations
- grouping of the heat generators into either the metallic or oxidic phases

- an aerosol generation model for material loss to the atmosphere above the melt.

Several features which are not incorporated in the present model, but are under consideration for possible future improvements, include:

- an aerosol transport model to describe the detailed movement of the heat generating material in the atmosphere above the melt and out to containment,
- a model defining the effects of core burnup on the decay heat curves,
- a model for the energy loss from the melt by gamma heating of the concrete, atmosphere, and surroundings and the attendant reduction in decay energy added to the melt.

All of these need considerable work. The latter two, in particular, must be studied further to assess the nature and magnitude of the effects involved and determine whether they warrant inclusion in the decay heat model.

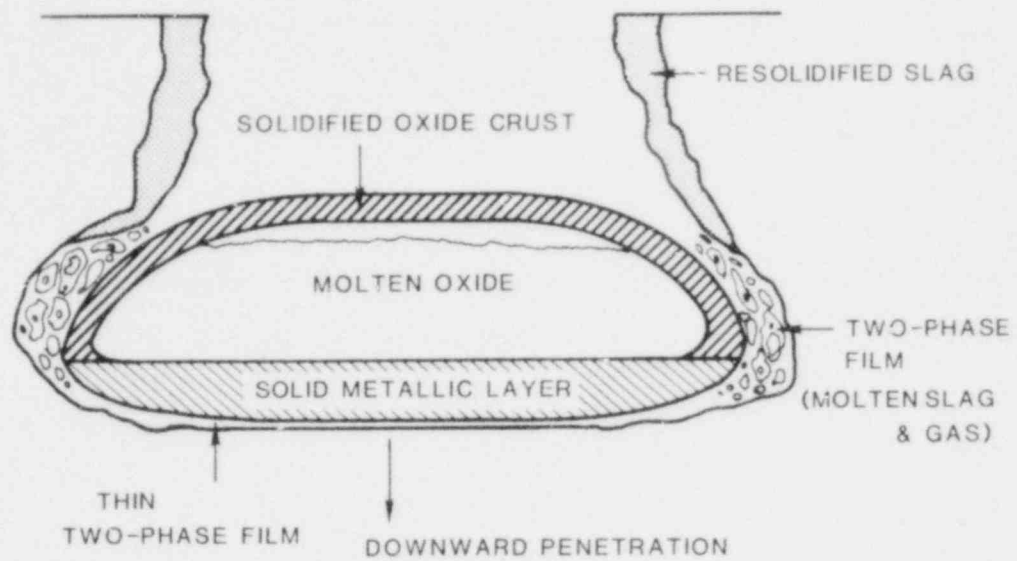
We want to determine the decay heat curves from as large a data base as possible. Unfortunately, the available literature contains few data in the time frame of interest here. For this reason, it was decided to use the SANDIA-ORIGEN code¹ to obtain decay power and mass concentrations for a 20-day period following shutdown. The core was assumed to be the same as that in a standard

Westinghouse large PWR plant in the equilibrium cycle, 80% capacity factor, prior to refueling. This represents the maximum expected decay heat generation. Subsequent calculations will be performed using other conditions between refuelings and a curve correction parameter determined.

1.2.4 Model for the Penetration of Concrete by a Hot Solid

A simple transient model for the penetration of a hot solid mass (e.g., core debris) into concrete was developed. The model considers the solidified core debris to be represented by a two-layer mass (oxidic and metallic phases, see Figure 1-1), each described by lumped-parameter properties (e.g., temperature). Energy generated within the solid by the fission product decay heat, \dot{Q}_{DH} , is transferred upwards by radiation and natural convection and sideways and downwards by conduction across a two-phase gas-molten concrete (slag) layer formed by ablation of the concrete. This simple model neglects sideways ablation of the concrete and just considers a constant slag-gas thickness, δ , due to downward ablation.

The energy balance equations for the metal and oxide are given by



CONCEPTUAL PICTURE OF SOLIDIFIED CORE
IN CONCRETE AFTER MELTDOWN

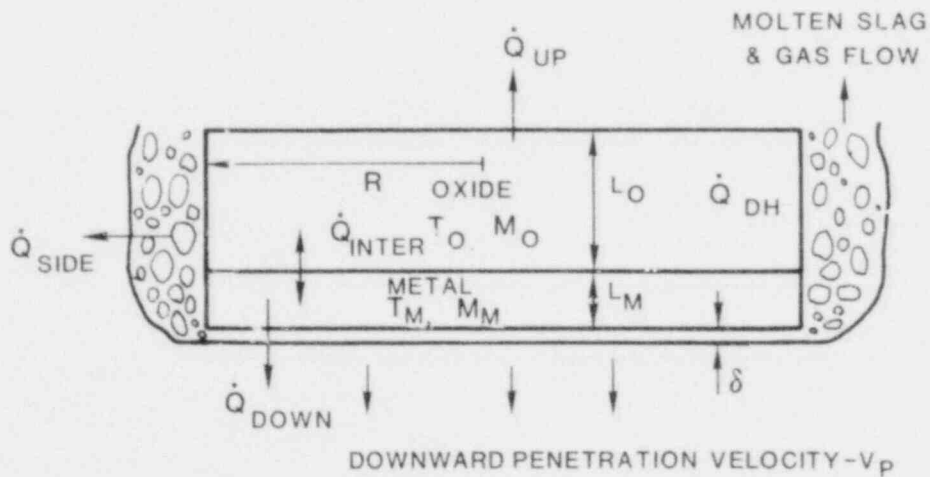


Figure 1-1. Concrete Penetration Model

$$m_o c_{p_o} \frac{dT_o}{dt} = \dot{Q}_{DH_o} - \dot{Q}_{INTER} - \dot{Q}_{UP} - \dot{Q}_{SIDE_o} \quad (1.1)$$

$$m_m c_{p_m} \frac{dT_m}{dt} = \dot{Q}_{DH_m} + \dot{Q}_{INTER} - \dot{Q}_{DOWN} - \dot{Q}_{SIDE_m} \quad (1.2)$$

The slag-gas film thickness beneath the solidified mass, δ , and velocity of downward penetration, V_p , are found by solving the following equations iteratively:

$$V_p = \frac{(m_o + m_m) g \delta^3}{8 \pi R^4 \mu_F} \quad (1.3)$$

$$\dot{Q}_{DOWN} = \rho_c V_p h_{ABL} \pi R^2 + \dot{Q}_{\text{cond. concrete}} \quad (1.4)$$

where

g is the gravitational acceleration = 9.8 m/s²

μ_F is the film viscosity = 1 kg/m s

ρ_c is the concrete density = 2400 kg/m³

h_{ABL} is the heated ablation of concrete = 2.5 x 10⁶ J/kg

$\dot{Q}_{\text{cond. concrete}}$ is the conduction into concrete given by the 1-D conduction equation for a semi-infinite body.

Initial results from preliminary calculations for a representative reactor-cavity/molten-pool geometry suggest four observations:

- (1) The controlling heat transfer resistances are those across the two-phase film layer and within the solidified core debris.
- (2) The oxide upper surface temperature is very low compared to the bulk temperature and this reduces the importance of radiation heat transfer.
- (3) The proportion of energy transferred upward and downward is approximately five times that transferred sideways. This is based on an assumed $(L_o + L_m)/R$ ratio of 1/3; however, the split between upward and downward heat transfer is still being investigated.
- (4) For the initial calculations, performed at a time where the core is predicted to be solid by CORCON calculations, it was found that the solidified core debris is not a stable configuration. As long as the total heat transfer rate out of the core debris is less than the volumetric heat generation rate, the core debris is not coolable and will reheat and remelt. This was found to be the case at an accident time of approximately 6 hours where the total heat loss rate was only 10% of the decay heat generation rate.

The significance of this final observation is that if these heat transfer rates from the solid core debris, ~1-2 MW, are representative of the long term interaction, the time to freezing of the melt without remelting is governed by the time required for the decay heat generation rate to decrease to the heat loss rate. Thus the stable freezing time could be on the order of months as opposed to the values of a few hours predicted by melt-concrete interaction computer models such as WECHSL and CORCON (which predict much higher heat transfer rates from the melt).

1.2.5 Viscosity of Two-Phase Mixtures

One aspect of melt/concrete interactions that must be addressed in modelling their long-term behavior is the crust formation and growth that occurs during solidification of the oxidic phase of the melt. Crust formation is expected to occur around the periphery of the melt (on the exposed surface of the slag layer and at the oxidic-phase/concrete interface) where temperatures are lowest. One material property that undoubtedly plays a significant role in the process of crust formation is viscosity. The viscosity of single phase siliceous melts increases dramatically with decreasing temperature. As the melt temperature falls below its liquidus, the precipitation of solids will produce a two-phase slurry having a viscosity different from that of the single phase melt because of the presence of the solid particulate.

The viscosities of molten siliceous materials have been correlated into an empirical formulation described by Bottinga and Weill.² This correlation has been implemented in a computer subroutine, VISRHO,³ that has been incorporated into the CORCON and WECHSL computer models of melt/concrete interactions. The subroutine provides density and viscosity data for siliceous melts of varying composition and temperature. The viscosity data provided by the subroutine are for single phase liquids.

Precipitation of solids in the siliceous melts will cause the viscosity of the resulting slurry to differ from that of the single phase melt. It is generally observed that such slurries are thixotropic. That is, the viscosity is a non-linear function of shear rate. The viscosity of a model thixotropic eutectic slurry as a function of shear rate is shown in Figure 1-2. This dependence of viscosity on shear rate is approximately exponential:

$$\eta = \eta_0 \exp(-\alpha \dot{\omega})$$

where

η = viscosity

η_0 = viscosity at zero shear rate

$\dot{\omega}$ = shear rate

α = parameter

The viscosity at zero shear rate is not the viscosity of the pure liquid. Rather it is the viscosity of the liquid-solid slurry.

Several correlations of the viscosities of slurries are available. For slurries containing less than 50 V/o solids, Kunitz⁴ has suggested

$$\frac{\eta_s}{\eta_l} = \frac{1 + 0.5\phi}{(1 - \phi)^4}$$

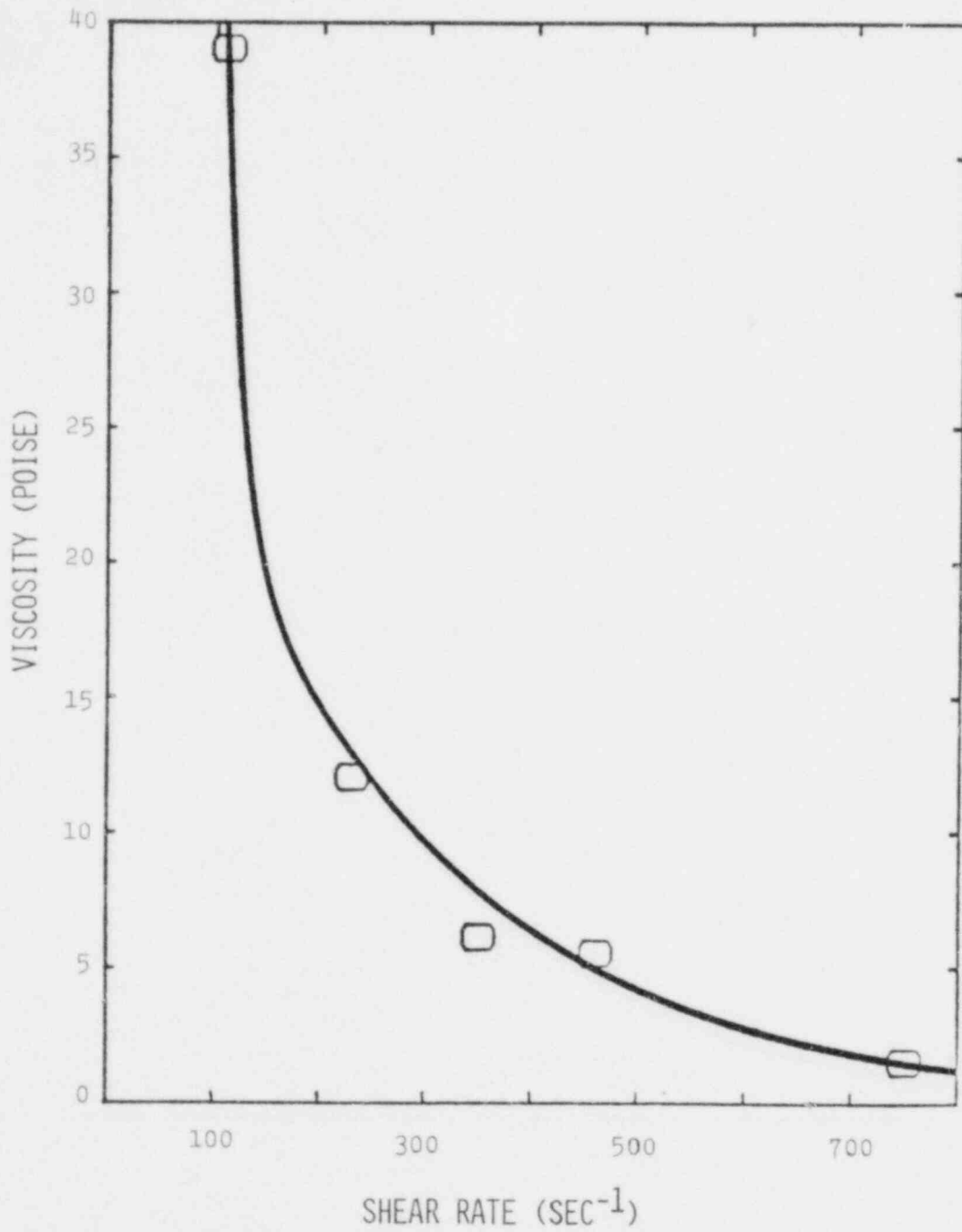


Figure 1-2. Shear Rate Dependence of Slurry Viscosity

where

η_s = viscosity of the slurry

η_l = viscosity of the pure liquid

ϕ = volume fraction of solids

Tiny and Luebbers ⁵ found the following correlations:

a) spherical particles, $\phi < 0.3$:

$$\frac{\eta_s}{\eta_l} = \left[\frac{1}{1 - \left(\frac{\phi}{0.46 - 0.00158(\eta_l/R)^{0.469}} \right)} \right]$$

b) cubic particles, $\phi < 0.4$:

$$\frac{\eta_s}{\eta_l} = \frac{0.403}{0.403 - \phi}$$

where

$$R = \rho_1 / \rho_l$$

ρ_1 = density of the particle.

Note that for all the correlations, viscosity increases as solid particles are added. Viscosities become quite large when the volume fraction of solids exceeds about 0.4. For a precipitating system of a typical binary oxidic mixture, a slurry of 40% solids could be achieved when the temperature of the system was the average of the solidus and liquidus temperatures at the bulk composition.

1.3 Acquisition of German Fuel Melt/Structural Materials Interactions Computer Codes

As part of an information exchange agreement between the United States and the Federal Republic of Germany (FRG), Mr. Vernon Badham, UCLA, visited Germany during the period May 5-16, 1980, under sponsorship of the NRC. The purpose of the trip was to expedite a NRC/BMFT (Bundesministerium fuer Forschung und Technologie) information exchange in the area of fuel-melt research. Mr. Badham delivered the U.S. developed MARCH and TRAP/MELT computer codes in exchange for a number of German computer codes which model various aspects of the interaction of molten core materials with reactor structural materials. Facilities visited during the trip included: the Kernforschungszentrum, Karlsruhe (KfK); Kraftwerk Union, Erlangen (KWU); and the Universität Hannover (UH). Computer tapes were obtained which contain the following German codes: WECHSL (KfK), KAVERN and BETZ (KWU), and THEKAR, HEMIS, BETON, BETSI, TEMBET and SACRI (UH). In addition, some documentation was obtained for most of these programs.

Mr. Badham stopped at Sandia for the week of May 19-23 on his return from Germany. The computer tapes and copies of all documentation were delivered to Sandia at this time. Mr. Badham also conducted an extensive review of the input and operating instructions for each code and assisted in the

set-up and check-out of the codes on the Sandia CDC 7600 computer. This activity has been completed. The various programs and data files have been made into permanent files on the CDC system and all programs have been successfully compiled. All but BETSI 3.1 are free of Fortran errors. BETSI 3.1 contains a number of special characters and type statements that are unacceptable on the CDC 7600. These would require further investigation to determine their intent and make them completely machine independent. Sample problem calculations have been made with those codes for which sample problem input data were provided. Finally, a tape containing the programs and data files is being prepared for shipment to UCLA.

The documentation supplied with the codes ranges from fairly complete technical reports in German, to technical journal articles and papers in English, to a collection of slides and viewgraphs. To facilitate the use of these codes by NRC and NRC contractor personnel, brief descriptions giving the essential features of the programs (to the extent possible with the available documentation) are provided in the following paragraphs.

WECHSL 6-10

- models the interaction between a pool of molten core materials and concrete
- two-dimensional, axisymmetric geometry

- arbitrary concrete cavity shape
- one-dimensional, quasi-steady-state concrete decomposition model including conduction in the solid matrix, convection in the gas phase, and indepth decomposition reactions
- two layered pool (metallic and oxidic phases) with internal heat generation
- melt/concrete interface modelled as a continuous gas film, bubbling into pool at horizontal and slightly inclined surfaces, and non-bubbling for steeply inclined surfaces
- oxidation of metallic elements by concrete decomposition gases passing through the melt

BETZ and KAVERN ⁶

- both model the interaction between a pool of molten corium and concrete
- two-dimensional, axisymmetric geometry
- arbitrary concrete cavity shape
- one-dimensional, quasi-steady-state ablation of concrete. KAVERN includes a model for heat conduction into the concrete
- melt is a homogeneous, isothermal mixture of metallic and oxidic phases with internal heat generation
- melt/concrete interface modelled as a gas felons. Three heat transfer models are available: bubble driven convection and free convection models developed at UH, and a gas film conduction model developed at KfK.
- metal/gas phase oxidation reaction is included

THEKAR codes 11-13

- five versions of the code were received: THEKAR-R, THEKAR-R2, THEKAR-H2, THEKAR-22, and THEKAR-ZYL. All model the transient thermal-hydraulics of a pool in a fixed geometry (i.e., non-ablating) container for the case of free convection driven by uniformly distributed internal heat generation. The coupled partial differential equations for the conservation of mass, momentum, and energy are solved numerically for different geometric and boundary conditions. A turbulent shear stress model is included in some of the codes to describe the turbulent mixing in the core region at high Rayleigh numbers. The fluid in the pool is treated as a single material (or mixture) having constant properties (except for density which is temperature dependent).
- THEKAR-R
 - two-dimensional, rectangular, geometry
 - equidistant grid spacing
 - low Ray number flows, no turbulent model
 - isothermal walls at the boundaries
 - addition of material to the pool is modelled by a stream entering the pool through its upper surface.
- THEKAR-R2
 - two-dimensional, trapezoidal or parallelogram geometry
 - otherwise, the same as THEKAR-R
- THEKAR-H2
 - two-dimensional, axisymmetric hemispherical geometry
 - non-uniform grid spacing
 - high Rayleigh number flows, turbulence model included.

- THEKAR-22

- two-dimensional, rectangular geometry
- non-uniform grid spacing
- high Rayleigh number flows, turbulence model included
- isothermal or adiabatic boundary conditions for each wall.

- THEKAR-ZYL

- two-dimensional, cylindrical geometry with a hemispherical bottom
- non-uniform grid spacing
- low Rayleigh number flows, no turbulence model
- isothermal or adiabatic boundary condition on cylindrical and spherical walls.

HEMIS 2.2

- models free convection flow in a pool with uniformly distributed internal heat generation
- two-dimensional, hemispherical geometry where pool depth can be less than the full hemisphere height
- non-uniform grid spacing
- low Rayleigh number flows, no turbulence model
- addition of material to the pool modelled as a stream flowing into the pool from above

BETON 3.5 & 3.6 14-16

- model the free convection flow in a pool containing two immiscible fluids where density differences may be induced by internal heat generation and/or different fluid properties
- two-dimensional, rectangular geometry
- equidistant grid spacing
- low Rayleigh number flows, no turbulence model
- isothermal or adiabotic boundary conditions, mass and heat transfer across upper and lower boundaries
- two-layered pool, one fluid in each
 - BETON 3.5 - lighter fluid over heavier fluid, stable configuration
 - BETON 3.6 - heavier fluid over lighter fluid, unstable configuration, Taylor instability produces "bubbles" of lighter fluid rising through the heavier layer

BETSI 2.4 & 3.1 17-19

- BETSI 2.4 computes the energy balance for a pool of molten core materials interacting with (and penetrating into) concrete. The energy flows treated are: melt/concrete heat transfer, radiation from the pool surface, energy absorbed by molten concrete entering the pool, and fission product decay heat generation. Three models are included for the melt/concrete heat transfer: an empirical correlation based on the Rinkleff experiments,¹⁷ the relation employed in BETON 3.6, and this same relation augmented with an empirical correlation to account for local surface inclination angle.
- two-dimensional axisymmetric geometry
- pool consists of a single material or mixture

- BETSI 3.1 is identical to BETSI 2.4 as far as the physical models are concerned. The only differences are that BETSI 2.4 is written for the CDC system while BETSI 3.1, which is used on a Prime computer, is written to be machine independent. In addition, BETSI 3.1 has less plotting capability than the 2.4 version.

TEMBET 1.2^{17,18}

- models the unsteady, one-dimensional heat conduction in decomposing concrete exposed to a high heat flux on one surface. It accounts for: the water, gas and energy releases associated with the various decomposition reactions within the concrete, the heat absorbed by the water as it passes out through the concrete, the effect of the water on the thermal conductivity, and melting at the heated surface.

SACRI¹⁷⁻¹⁹

- models the penetration of a pool of molten core materials into dehydrated sacrificial materials that are soluble in the melt (properties for basalt are built in). It is similar to the BETSI code and uses some of its subroutines.
- two-dimensional, rectangular and axisymmetric geometries.
- pool may consist of either a homogeneous melt or a two layer (oxidic and metallic phases) melt.
- heat transfer from all surfaces (of pool) modelled using empirical correlations for free convection at high Rayleigh numbers.

1.4 References

- ¹D. E. Bennett, SANDIA-ORIGEN User's Manual, SAND 79-0299 (NUREG/CR-0987), Sandia National Laboratories, Albuquerque, NM (Oct. 1979).
- ²Y. Bottinga and D. F. Weill, "The Viscosity of Magmatic Silicate Liquids: A Model for Calculation," American Journal of Science, Vol. 272, pp. 438-475 (1972).
- ³D. A. Powers and A. W. Frazier, VISRHO: A Computer Subroutine for Estimating the Viscosity and Density of Complex Silicate Melts, SAND76-0649, Sandia National Laboratories, Albuquerque, NM (June 1977).
- ⁴Kunitz, Journal General Physiology, Vol. 9, p. 715 (1926).
- ⁵Ting and Leubbers, American Institute of Chemical Engineering Journal, Vol. 3, p. 111, (1957).
- ⁶Experimente zur Simulation Grosser Kernschmelzen in Wechselwirkung mit dem Reaktorbeton, PNS 4323, Kernforschungszentrum Karlsruhe, Kraftwerk Union and Technische Universität Hannover (Feb. 1978).
- ⁷H. Alsmeyer and M. Reimann, "On the Heat and Mass Transport Processes of a Horizontal Melting or Decomposing Layer Under a Molten Pool", Nuclear Reactor Safety Heat Transfer, The Winter Annual Meeting of the ASME, Atlanta, Ga., pp. 47-53 (Nov. 27-Dec. 2, 1977).
- ⁸H. Alsmeyer, et. al., A Model Describing the Interaction of a Core Melt with Concrete, NUREG/TR-0039, Washington, D. C., U. S. Nuclear Regulatory Commission, (Sept. 1978). (Translation of KfK 2395, Kernforschungszentrum Karlsruhe, FRG (Oct. 1977)).
- ⁹M. Reimann, W. B. Murfin, and H. Alsmeyer, "On the Penetration of Hot Melts into Concrete Structures", Trans. of the ANS, Vol. 31, ENC '79 Conference, Hamburg, FRG, pp. 371-373 (1979).
- ¹⁰M. Reimann and W. B. Murfin, "Calculations for the Decomposition of Concrete Structures by a Molten Pool", Europ. Appl. Res. Rept., Vol. 1, No. 6, pp. 1554-1566 (1979).

- 1¹ F. Mayinger, et. al., Examination of Thermohydraulic Processes and Heat Transfer in a Core Melt, BMFT-RS48/1 (Translation), Technische Universität Hannover, FRG (July 1975).
- 1² U. Steinberner, Untersuchungen zur Schmelzpoolstabilisierung, BMFT-FB (RS 166-79-05) Band II B, Universität Hannover, FRG (April 1979).
- 1³ H. H. Reineke, Numerische Untersuchung der Thermohydraulischen Vorgänge und des Wärmeübergangs in einer Kernschmelze bei Kugelsegmentförmiger Geometrie and bei Zufließendem Material von Oben, BMFT-FB (RS 166-79-05) Band II A1, Universität Hannover, FRG (June 1979).
- 1⁴ F. Mayinger, et. al., Verhalten der Kernschmelze beim Hypothetischen Störfall, BMFT RS 165, Technische Universität Hannover, FRG (1975).
- 1⁵ F. Mayinger, et. al., Behavior of the Core Melt-Down in Case of a Hypothetical Malfunction, BMFT RS 166, Technische Universität Hannover, FRG (1976). Translated by SCITRAN, U. S. NRC (July 1978).
- 1⁶ R. Schramm, Berechnung von Konvektionsformen bei Unmischbaren Fluiden mit Inneren Wärmequellen, Dissertation, Universität Hannover, FRG (1979).
- 1⁷ F. Mayinger, et. al., Contribution of the Institut für Verfahrenstechnik der Universität Hannover, Collection of slides shown at the Core Melt Review Meeting, July 12-13, 1979, Hannover, FRG.
- 1⁸ F. Mayinger, et. al., Verhalten der Kernschmelze beim Hypothetischen Störfall, BMFT RS 166, Technische Universität Hannover, FRG (1977).
- 1⁹ F. Mayinger, et. al., Theoretische und Experimentelle Untersuchung des Verhaltens eines Geschmolzenen Kerns im Reaktorbehälter und auf dem Betonfundament, BMFT-FB (RS 166-79-05) Band V, Universität Hannover, FRG (Feb. 1980).

2. Steam Explosion Phenomena
(M. L. Corradini, D. E. Mitchell, L. S. Nelson)

The two main purposes of the steam explosion phenomena program are: (1) To identify experimentally the magnitudes and time characteristics of pressure pulses and other initial conditions which are necessary to trigger and to propagate explosive interactions between water and molten Light Water Reactor (LWR) core materials; and (2), to assess the probability and consequences of steam explosions during hypothetical meltdown accidents in LWRs. The major efforts in this program encompass four areas:

- (i) Small scale experiments using simulant molten materials (Corium A, E, Iron-oxide, 1-10 g) with water. These experiments are directed toward understanding a) the applied triggering pressures needed to induce vapor explosions, b) the conversion of heat to work under a variety of initial conditions, and c) the characteristics of the fuel debris from such events.
- (ii) A large-scale, closed-geometry, fully instrumented test series using induction- and thermite-generated melts (Iron-oxide, iron-alumina, Corium-E, 2-25 kg) dropped into water. These experiments investigate, at large scale and with prototypic melts, the thermal-to-mechanical energy conversion ratio and the propagation of the explosion as functions of fuel and coolant temperatures, mass ratios and compositions. These tests may also address the slower steam production which results when molten fuel is submerged in the water without the occurrence of a steam explosion.
- (iii) Modelling and analysis of steam explosions. This theoretical work will interpret the

observed experimental results in light of past theories and models of steam explosions (vapor explosions) and will develop and test new theories and models where necessary. The ultimate objective is to be able to relate the experimental results to the possible behavior of steam explosions during meltdown accidents. The analysis also addresses the effects of the meltdown sequence on the explosion.

- (iv) Structural consequences of the steam explosion. This work is directed toward (1) evaluating how a steam explosion might lead to containment failure via missile generation or other mechanisms, (2) identifying the realistic mechanisms that could dissipate the explosion energy and reduce the probability of containment failure, and (3) understanding how the explosion might fit into the overall accident progression.

2.1 Summary

A brief summary of the research accomplishments during the third quarter of fiscal 1980 is presented in the following sections

2.1.1 Small Scale Experiments

Progress was made in several areas this quarter. The initial single droplet experimental series was completed. This test series improved the laser melting and data acquisition techniques. A number of very reproducible experiments were performed and the data were submitted to the CSNI for an international interpretive exercise. A new high pressure chamber was fabricated to conduct single droplet tests at high ambient pressures (~1 MPa). The apparatus is currently being checked out for operational safety. Finally, the second test series is nearing completion. This set of experiments is designed

to determine the trigger threshold for a specific set of initial conditions.

2.1.2 Fully Instrumented Test Series

The FITS experimental program accomplished three tasks this quarter:

- i) the second in-chamber experiment, FITS2A, was successfully conducted,
- ii) two exo-FITS experiments MD-17 and -18 were performed,
- iii) fuel particle size data were obtained for the tests FITS1A and FITS2A.

The FITS2A test resulted in a violent spontaneous explosion before the melt was fully submerged in the water. Subsequent exo-FITS tests MD-17 and MD-18 together with past tests, indicated that melt entry velocity may be a key parameter in determining if and when a spontaneous explosion will occur. This is in agreement with the small scale test results of Nelson. FITS1A and 2A particle size data indicated that the mean particle diameter (~200 μm) with a violent explosion occurring is much smaller than that diameter (~3000 μm) for the case with no violent explosion.

2.1.3 Modelling and Analysis of Steam Explosions

During this quarter three topics were investigated: (1) modelling of the core meltdown accident progression using both simple analysis and MARCH, the Battelle-Columbus

computer meltdown model; (2) continued development of the transient 1-D explosion model in WONDY and modelling the exo-FITS test; and (3) determination of the initial conditions for the explosion for use in a fluid-structural 2-D calculation.

The first task is a continuation of the work begun last quarter, i.e., an investigation of the core meltdown accident progression to better understand the key phenomena and how steam explosions may affect or be affected by them. Preliminary analysis indicated that if an ex-vessel steam explosion did occur, the effect on the containment would be a static pressure rise of less than 0.1 MPa. A further pressure rise may occur as the core debris heats the containment atmosphere directly as well as producing more steam by prolonged boiling. If an ex-vessel steam explosion does not occur, containment pressurization would be reduced by the formation of a debris bed in the reactor cavity which could limit the water boiloff rate.

The 1-D transient explosion model was used to investigate the macroscopic effects of changing the trigger magnitude, and the volume fractions of fuel and coolant in the explosion zone. In conjunction with this effort, work began on constructing an empirical model for the steam explosion to be used in 2-D fluid-structure calculations. Initial results indicate that water can be

described approximately using the analytic equation of state model which is part of the 2-D hydrodynamic codes at Sandia.

2.1.4 Structural Consequences of the Steam Explosion

During this quarter the calculations performed for the Zion-Indian Point Study were reviewed and the writing of the second interim report on the assessment of containment failure via steam explosions began.

2.2 Single-Drop Steam Explosion Studies With Molten Iron Oxide

During this quarter, improvements in the single drop laser melting techniques were made to permit better photographic resolution and control of the distance the drop falls to the surface of the water.

The effect of drop fall distance on the steam explosions was studied. It was found that air could be entrained with the drop as it entered the water, adding to the volume of the vapor layer that surrounded the hot drop. By using short fall distances (~10 mm), it was possible to minimize entrained gas. When this was done, spontaneous (non-triggered) explosions resulted (melt temperature in excess of 2000 K). With slightly longer fall heights (15-20 mm), a small amount of gas was entrained around the drop and the drop did not explode

until a pressure transient was added. In the same experiments, it was possible to estimate the thickness of the boiling film to be ~0.3 mm, for a drop height of 15 mm.

The effect of the magnitude of the initiating pressure transient on steam explosion triggering was also studied. For the set of interaction conditions used here, the threshold peak pressure was 0.3 to 0.5 MPa.

Particle size distributions were determined for the debris produced in spontaneous and triggered explosions. Median mass averaged particle diameters were in the range 100-125 μm .

Data packages were supplied to 13 agencies as part of a world-wide exercise to interpret Sandia's steam explosion experiments performed with single drops of molten iron oxide. This exercise is sponsored by the International Committee on Safety in Nuclear Installations (CSNI).

A new high pressure chamber has been fabricated for studying single laser melted drop explosions at ambient pressures up to 1.0 MPa.

2.2.1 Techniques

Several apparatus modifications were made to improve the single drop experiments. These included rearranging

the cameras to achieve higher framing rates and better image resolution, and installing a new polymethylmethacrylate interaction chamber. This chamber permitted easier retrieval of debris, better photographic images, and the ability to be filled with water to the very top, permitting CO₂ laser heating of the drop as close as 8 mm above the water surface.

Data were gathered to determine the rate of dissolution of the 0.25 mm diameter iridium wire support on which the iron oxide drops are melted. The weights of the same iridium wire used over a span of 17 experiments were plotted against experiment number, as shown in Figure 2-1. From this plot, it is seen that an average of 0.11 mg of iridium is incorporated in each 50 mg molten iron oxide drop. The effect of this amount of iridium on the properties of the melt is considered negligible.

2.2.2 Effect of Drop Fall Distance Gas Entrainment

In the experiments with single drops of molten iron oxide started last quarter, the films showed a "bag" of gas and vapor approximately 8 mm tall attached to the top of each drop as it descended through the water. Explosions could be triggered with these drops with bridgewire pressure transients of 0.75-0.85 MPa peak pressure. In these new experiments, the drops fell

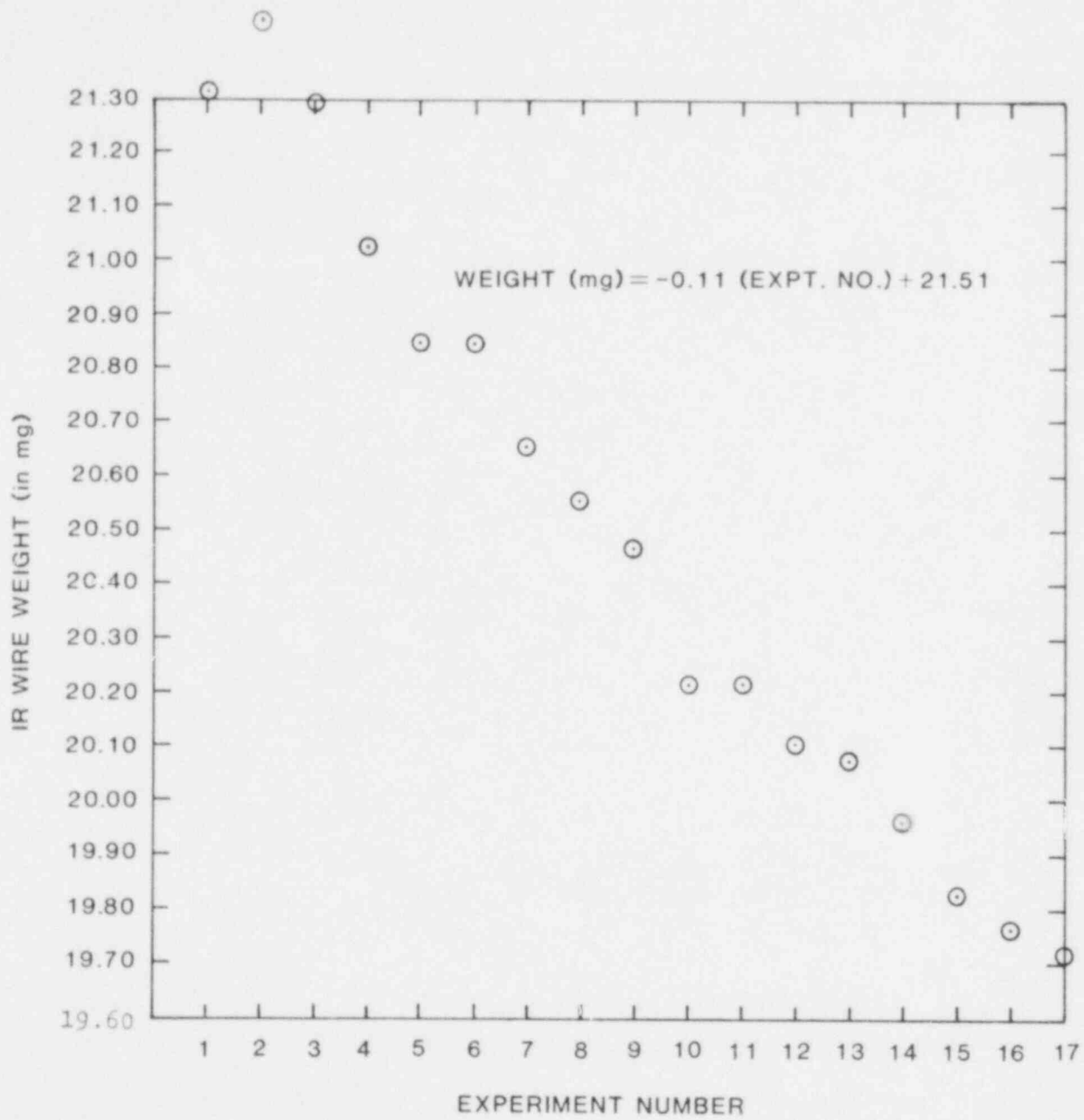


Figure 2-1. Iridium Wire Weight Loss for Seventeen Experiments

approximately 50 mm before entering the water surface. In earlier scoping experiments, where the drop fall distance was approximately 10 mm, the "bags" were not observed. A sequence of experiments was performed in which drop fall distance was decreased from 50 to 8 mm in several steps to determine whether the "bag" could be prevented from forming. The gas "bags" observed with droplets in the water are reproduced in Figures 2-2, 2-3 and 2-4 for 50, 20 and 15 mm fall heights respectively. Note that the "bags" essentially disappear at drop heights of 15 to 20 mm. These drops were also triggered to explode with similar bridgewire transients.

However when the fall distance was decreased to 8-11 mm, the drops of molten iron oxide exploded spontaneously (without the application of a pressure transient). The spontaneous explosions observed here have occurred at high melt temperatures, probably in excess of 2000 K, (the initial temperature of the drops before release is 2233 K).

Boiling Film Thickness

The almost circular image with very low entrained gas shown in Figure 2-4 yielded an estimate of the vapor film thickness. This was accomplished by measuring the width of the optical image and subtracting from it the diameter of the drop calculated from its weight and the

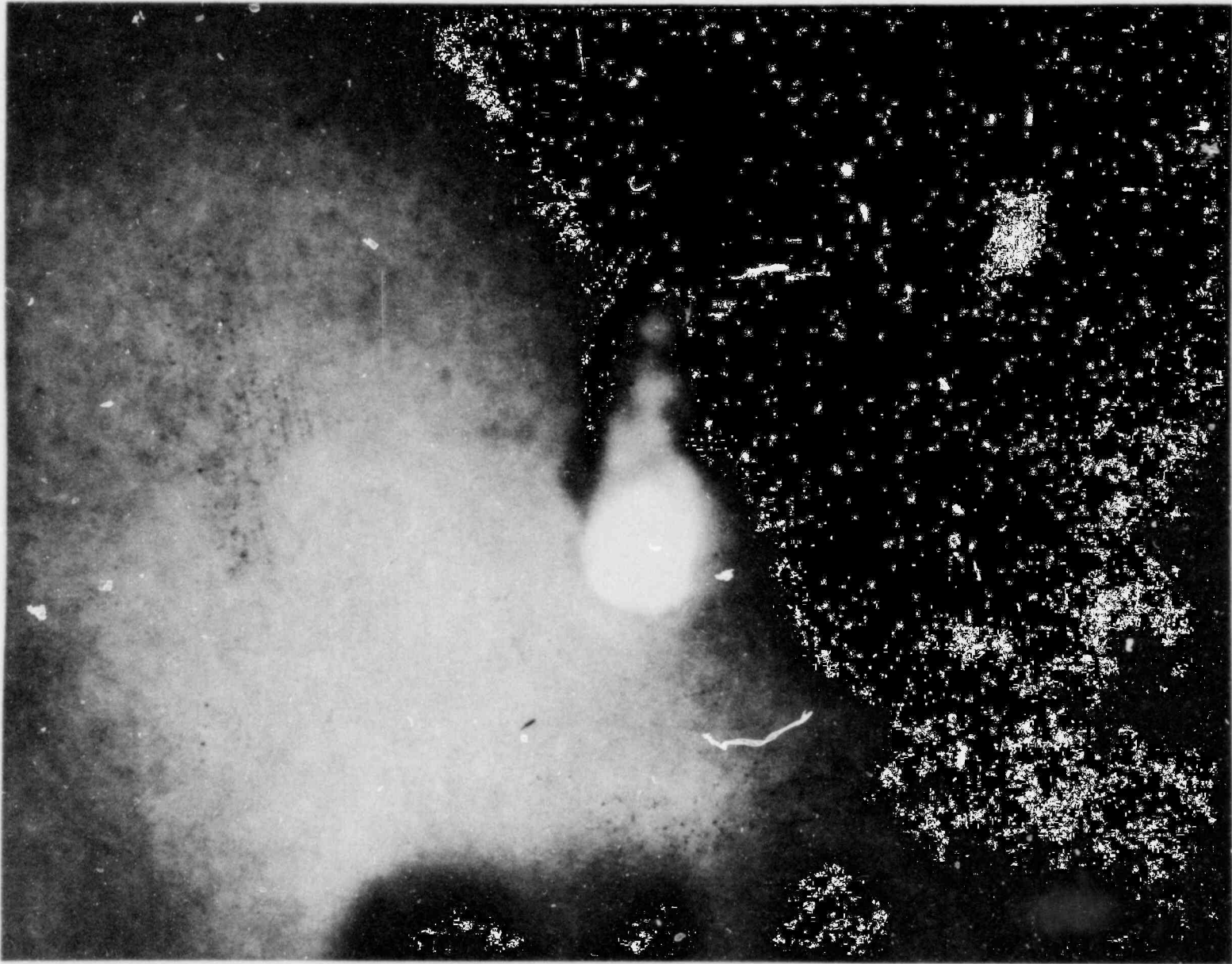


Figure 2-2. Single frame reproduced from film of iron oxide drop descending in water prior to triggered explosion. Drop (brightly luminous image) is 2.7 mm in diameter. Drop had fallen 50 mm before entering the water. Note "bag" approximately 8 mm tall above the drop as it descends. (11-68-1-1)

POOR ORIGINAL

POOR ORIGINAL

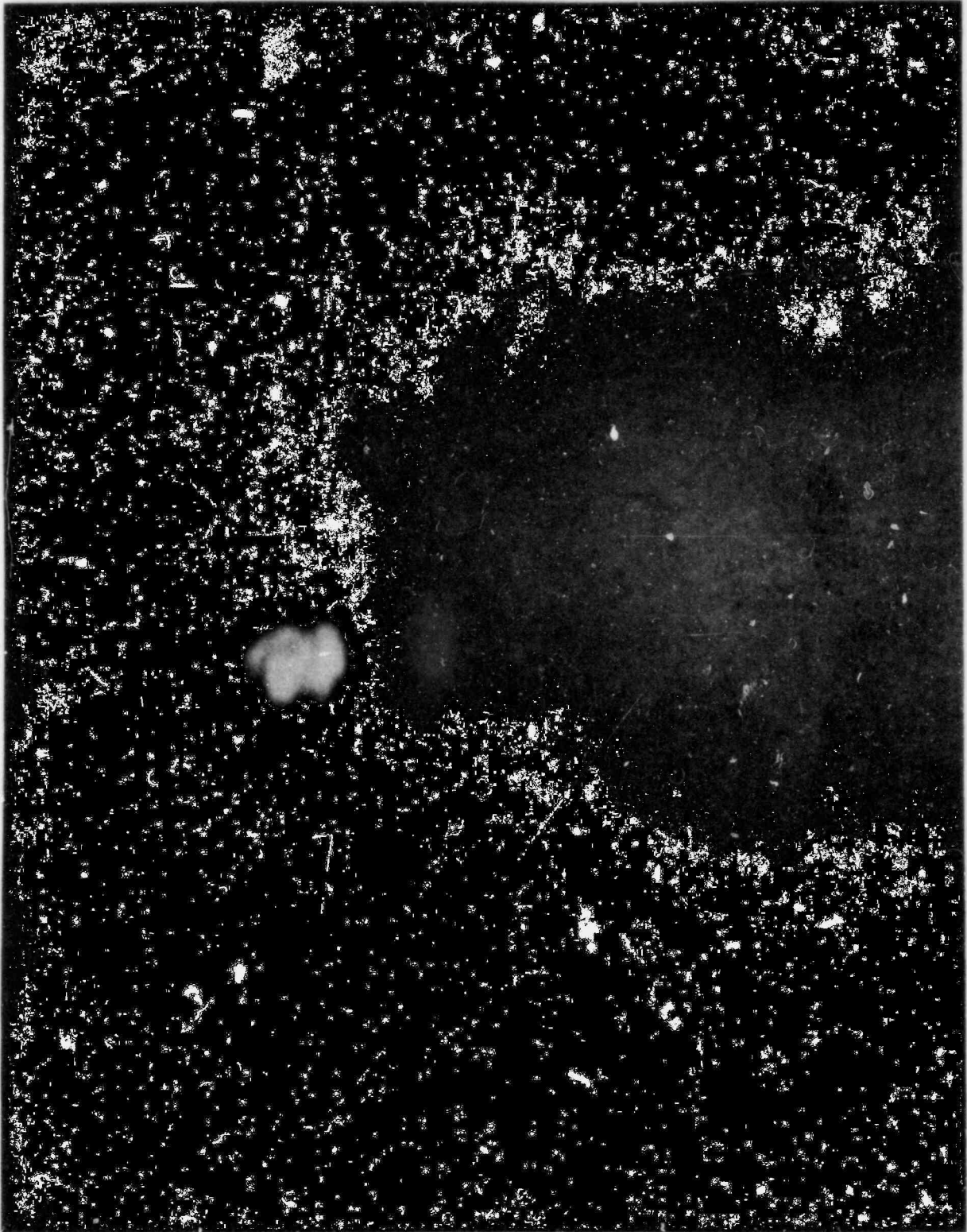


Figure 2-3. Same conditions as in Figure 2-2, except that drop had fallen 20 mm before entering the water. Note greatly reduced "bag" above the drop. (11-74-2-1)

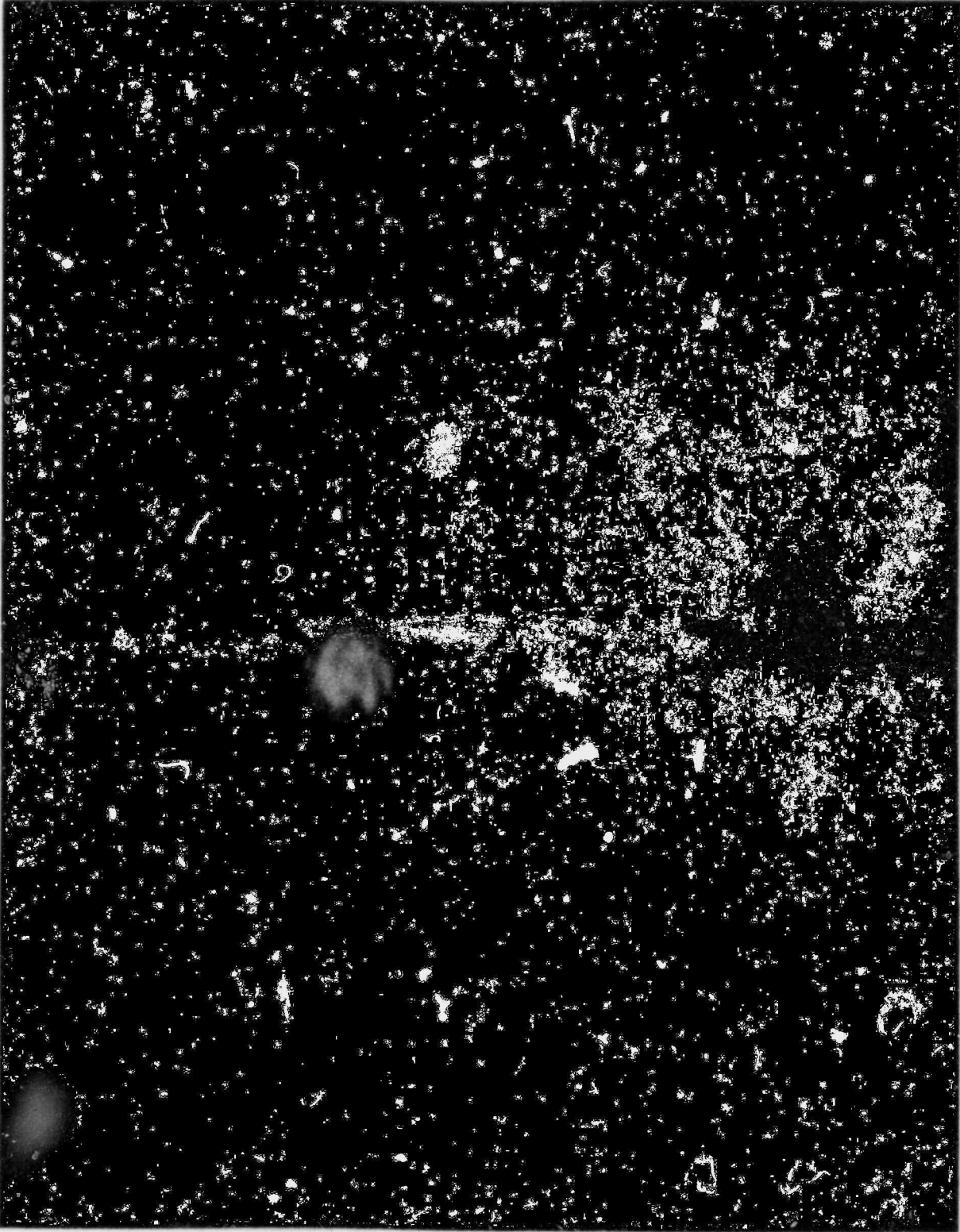


Figure 2-4. Same conditions as in Figures 2-2 and 2-3, except that drop had fallen 15 mm before entering the water. Note that "bag" is essentially absent here. (11-75-2-1)

known density of the melt. As an example, for experiment 11-74-2, the image diameter was 3.33 mm for a drop with mass of 0.05483 g. Using the density of 4.85 g/cc for molten Fe_3O_4 (Reference 1), the drop diameter was estimated to be 2.79 mm, giving a vapor film thickness of 0.27 mm. This film thickness occurred at a local atmospheric pressure of 0.083 MPa in water subcooled by 70 K.

2.2.3 Effect of the Magnitude of the Trigger Transient

The pressure transient to which the molten iron oxide drop was exposed was reduced by increasing the bridgewire-to-drop distance. A polymethylmethacrylate vessel 450 mm tall and 152 mm on a side was used to perform the experiment. The iron-oxide drop initial conditions were identical to previous experiments ($T_f = 2200$ K, $D_f = .0027$ m, drop height 15-20 mm).

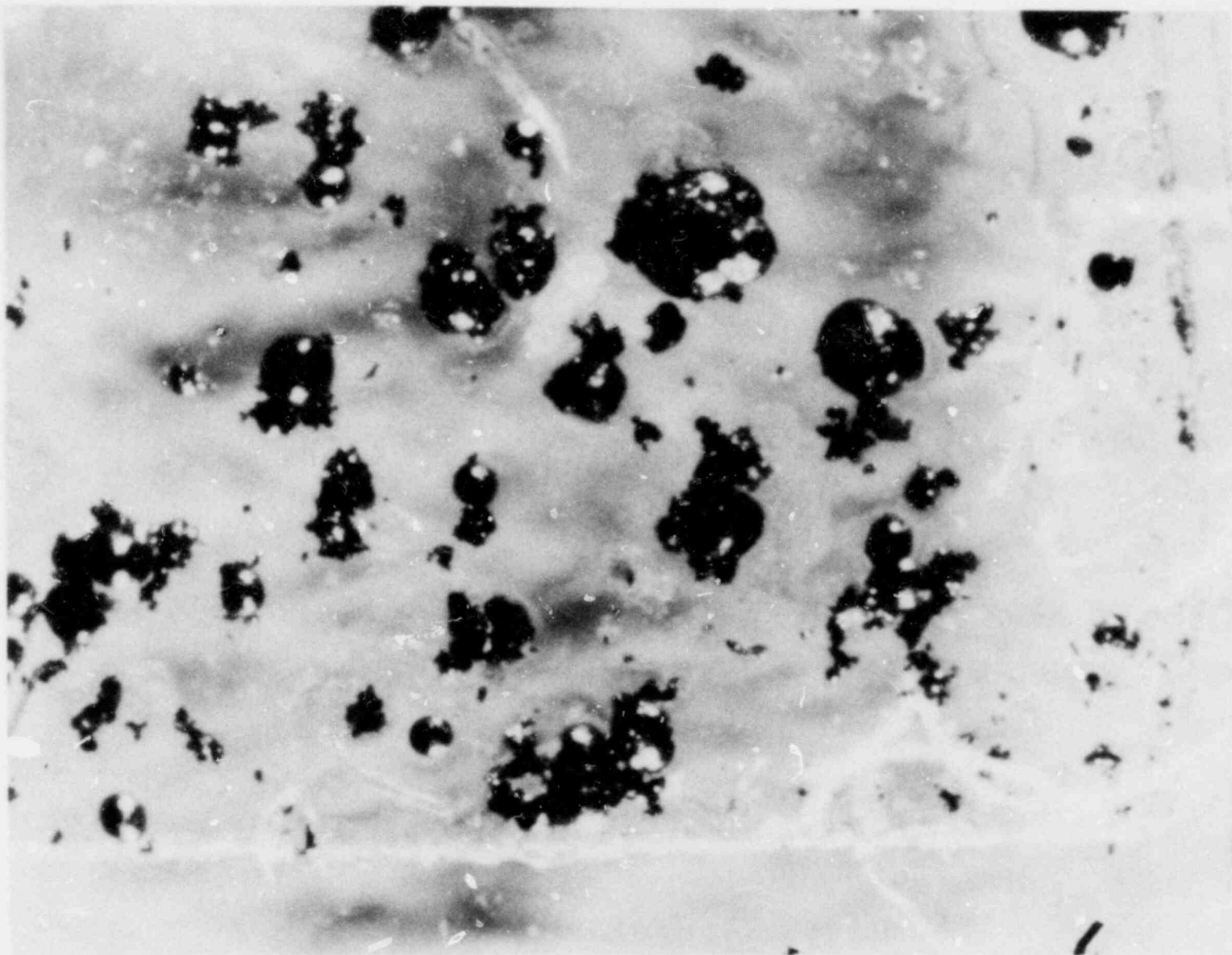
When the bridgewire was placed at the bottom of the interaction vessel, the peak pressure transient measured near the drop was 0.05 MPa. A drop exposed to this pressure transient failed to explode. The bridgewire was then raised progressively in the tank to increase the peak transient pressure. At 0.19 MPa, some relatively large tongues of melt were ejected approximately 0.1 s after the bridgewire was fired, but no explosion occurred. At 0.26 MPa, the drop image undulated somewhat and then exploded about 100 ms later. As the pressure transient increased still further the period of undulation decreased

and explosions occurred at shorter and shorter intervals until the threshold at about 0.5 MPa. At this point the explosions occurred promptly, within one or two ms of firing the bridgewire.

2.2.4 Debris Characterization

Debris particles from a triggered (11-75-1) and a spontaneous (11-72-2) explosion with molten iron oxide were analyzed. After the explosions, the debris particles were separated from the water by filtration with a cellulosic fiber filter paper. When the particles produced in such an experiment were arrayed over a 38.5 cm² area, the particle density was too high for proper measurements. In order to reduce the particle density, a piece of transparent mending tape was pressed over portions of the debris on the dried filter paper. After stripping the tape, it was found that reasonable particle densities for counting were achieved on both tape and paper.

In order to measure the particles, photographs were taken of corresponding areas on both tape and filter paper with approximately 50 X magnification. Typical photographs are shown in Figures 2-5 and 2-6 for the debris from the spontaneous explosion. The individual particle images were then sized with Zeiss model TG23 particle size analyzer. The particle size histograms so obtained were converted to mass fractions by adding the information from both tape and filter paper, using a



POOR ORIGINAL

Figure 2-5. Photomicrograph of debris collected from spontaneous steam explosion of molten iron oxide drop in water. This portion of the debris was removed from the filter paper with transparent mending tape. Bar is 0.2 mm long. (11-72-2)

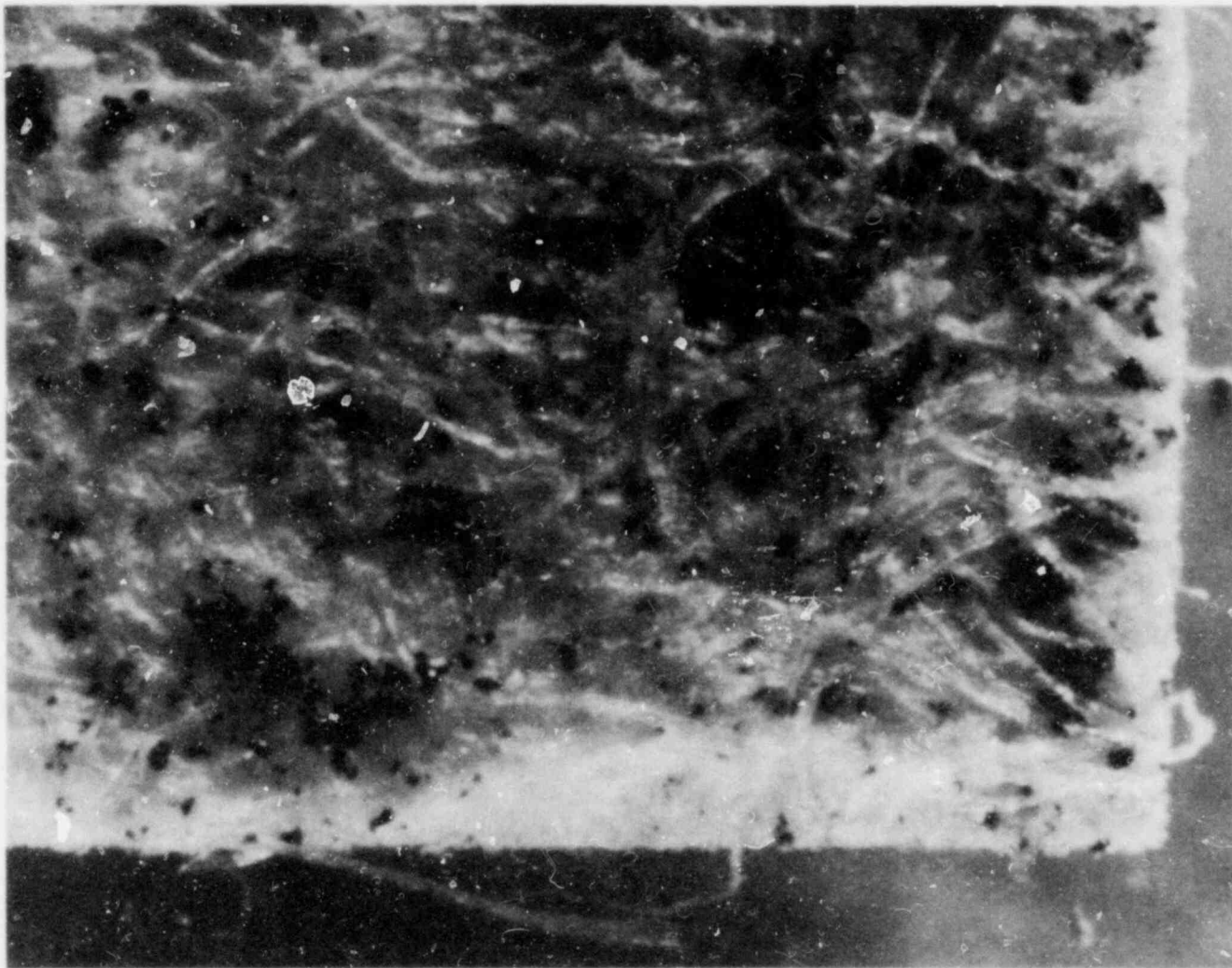


Figure 2-6. Same as Figure 2-5, except that this image shows the corresponding filter paper from which the debris in Figure 2-5 was removed. Bar is 0.2 mm long. (11-72-2)

POOR ORIGINAL

density of 5.18 g cm^{-3} solid Fe_3O_4 (Reference 2). Plots of the cumulative particle size fractions from the spontaneous and the triggered explosions are shown in Figures 2-7 and 2-8. Also shown on these plots are the smallest particle sizes observed by Mizuta (RUN 24) for molten uranium dioxide poured into liquid sodium (Reference 3). Note that the particle sizes obtained here are considerably smaller than those observed by Mizuta.

The particle sizes determined in these two experiments were converted to geometrical surface areas, assuming perfectly spherical dense Fe_3O_4 particles. The calculated surface areas were $0.3 \text{ m}^2\text{g}^{-1}$. The surface areas determined by gas absorption with exploded arc melted corium simulant debris were on the order of 0.2 to $1.0 \text{ m}^2\text{g}^{-1}$ (Reference 4). This suggests that the explosions were of comparable intensity in both apparatuses.

2.2.5 Interpretive Study of Steam Explosion Data

During this quarter, data packages were sent to 13 interested agencies in an international exercise to interpret Sandia's steam explosion experiments performed with single drops of molten iron oxide. This exercise is sponsored by the International Committee on Safety in Nuclear Installations (CSNI), with participation by special invitation of the committee.

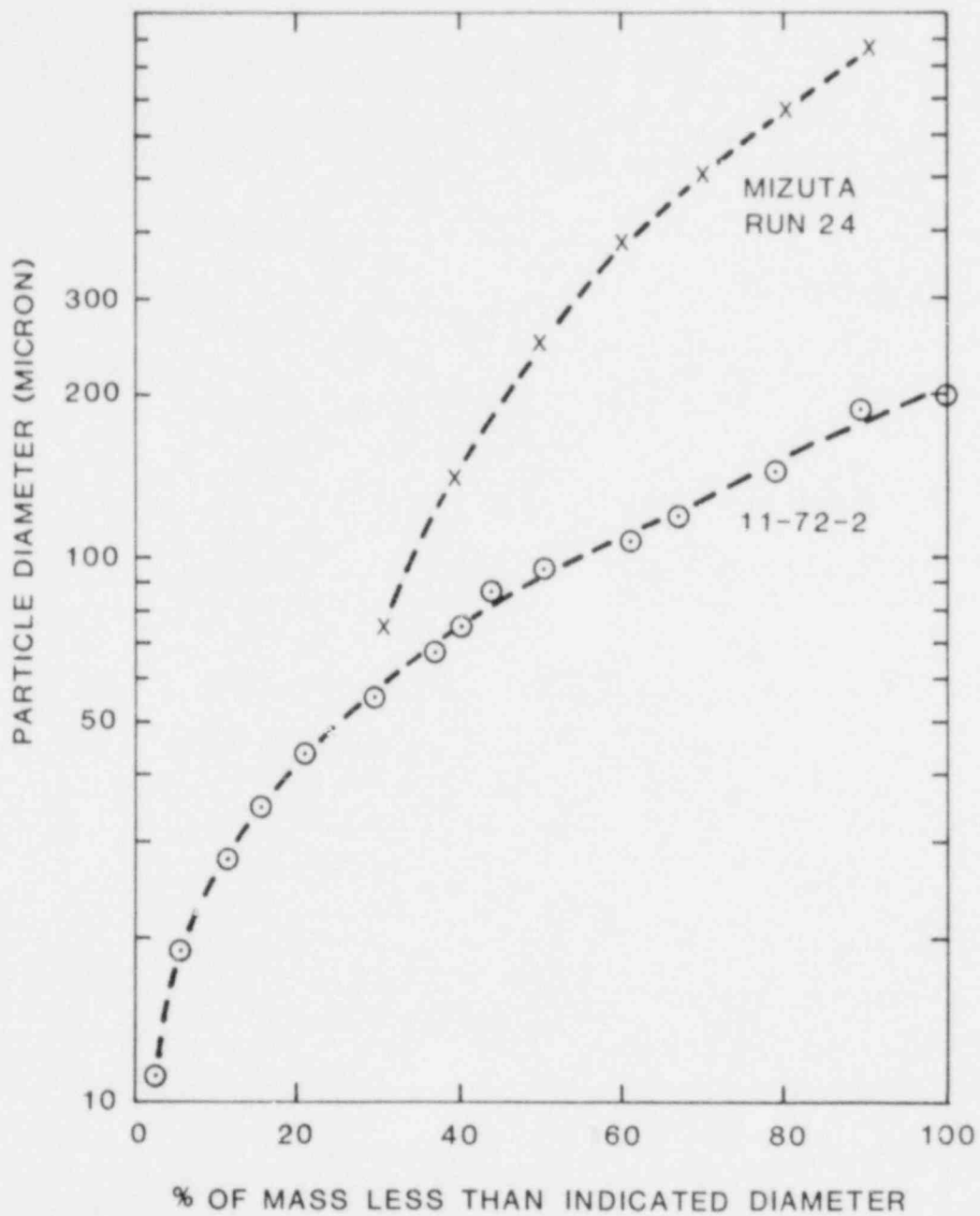


Figure 2-7. Particle diameters of debris shown in Figures 2-5 and 2-6, shown as a function of cumulative weight fractions of the debris.

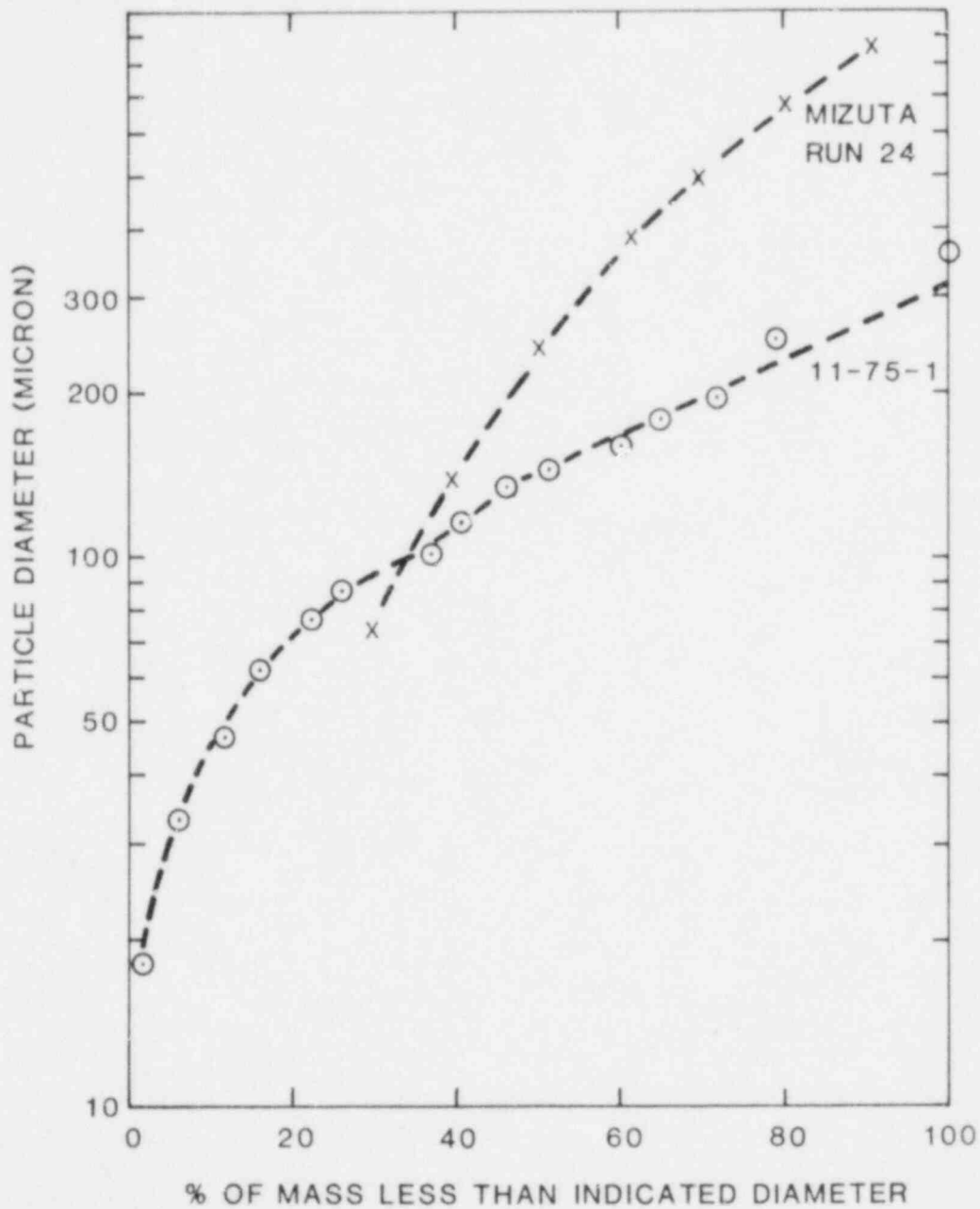


Figure 2-8. Particle diameters of debris from triggered explosion of molten iron oxide drop in water, shown as a function of cumulative weight fractions.

The data package contains a high speed film, pressure records, and a table of 22 parameters known or measured for each of five explosive iron oxide-water interactions (see Table 2-I). Each agency will analyze the data over a period of approximately six months in preparation for an information exchange meeting later in 1980.

2.2.6 Experiments at Elevated Pressures

An apparatus was constructed for performing the single drop laser melting experiments at ambient pressures up to 1.0 MPa. The apparatus is currently being checked for operational safety. A sketch of the apparatus is shown in Figure 2-9.

2.3 Fully Instrumented Test Series

During this quarter the second in-chamber experiment, FITS2A, was conducted, and particle size data were obtained from FITS1A and 2A. Also two exo-FITS experiments MD-17 and MD-18 were done.

Based on information obtained from FITS1A a second in-chamber experiment was designed. FITS1A failed to generate a spontaneously triggered explosion. This was probably due to the higher than normal entry velocity and a mass (2 kg) close to the threshold for spontaneous explosions based on earlier exo-FITS experiments. Because of these reasons an adjustment in crucible delivery velocity was made and the melt mass was increased

TABLE 2-1

Experimental Parameters for Interactions Between
Single Drops of Molten Iron Oxide and Liquid Water

Experiment Number : →	11-74-1	11-74-2	11-75-1	11-75-2	11-76-1
Melt Temperature (K)	2233	2233	2233	2223	2233
Melt Atmosphere	Air	Air	Air	Air	Air
Mass FeO _x (g)	0.05483	0.05523	0.05460	0.05530	0.05461
Melt Composition (O/Fe)	1.34	1.32	1.28	1.34	1.32
Drop Diameter (mm)	2.78	2.79	2.78	2.79	2.78
Coolant Identity ¹	H ₂ O	H ₂ O	H ₂ O	H ₂ O	H ₂ O
Coolant Subcooling (K)	70.0	69.5	71.0	70.5	69.5
Additives to Coolant	None	None	None	None	None
Chamber Dimensions (length, width, height) (mm)	152x152x152	152x152x152	152x152x152	152x152x152	152x152x152
Coolant Depth (mm)	160	149	159	160	160
Ambient Pressure (MPa)	0.0830	0.0836	0.0836	0.0833	0.0833
Drop Fall Distance above Coolant (mm)	19	22	23	16	15
Drop Fall Time above Coolant Surface (ms)	62	60	62	52	45
Drop Velocity upon Insertion (mm/ms) ²	0.61	0.59	0.61	0.51	0.44
Drop Dwell Time in Coolant before Initiation (ms)	119	119	126	137	124
Drop Velocity before Initiation (mm/ms) ³	0.32	0.23	0.38	0.32	0.32
Drop Depth at Initiation (mm)	50	49	55	67	60
Initiation Pulse (a) Rise Time (μs)	6	6	6	6	6
(b) Pulse Width at 1/e (μs)	18	14	14	14	14
(c) Peak Pressure at Drop (MPa) ⁴	0.64	0.68	0.71	0.86	0.72
(d) Frequency of Pulsation	1 Pulse	1 Pulse	1 Pulse	1 Pulse	1 Pulse
Drop to Bridgewire Distance at Initiation Time (mm)	76	70	72	63	71
Drop to Transducer Distance at Initiation Time (mm)	50	50	49	42	45
Bridgewire to Transducer Distance (mm)	49	49	49	47	47
Vapor Film Thickness (mm) ⁵	0.27	0.27	0.27	0.27	0.27

¹Deionized water was boiled for thirty minutes and cooled in ice just before each experiment.²Calculated from the acceleration of gravity and the fall time.³Measured from high magnification films.⁴Peak Pressure at the drop was estimated.⁵The vapor film thickness was determined from the difference between the drop diameter (estimated from the drop weight and published melt density) and the diameter of the drop image on the high magnification films.

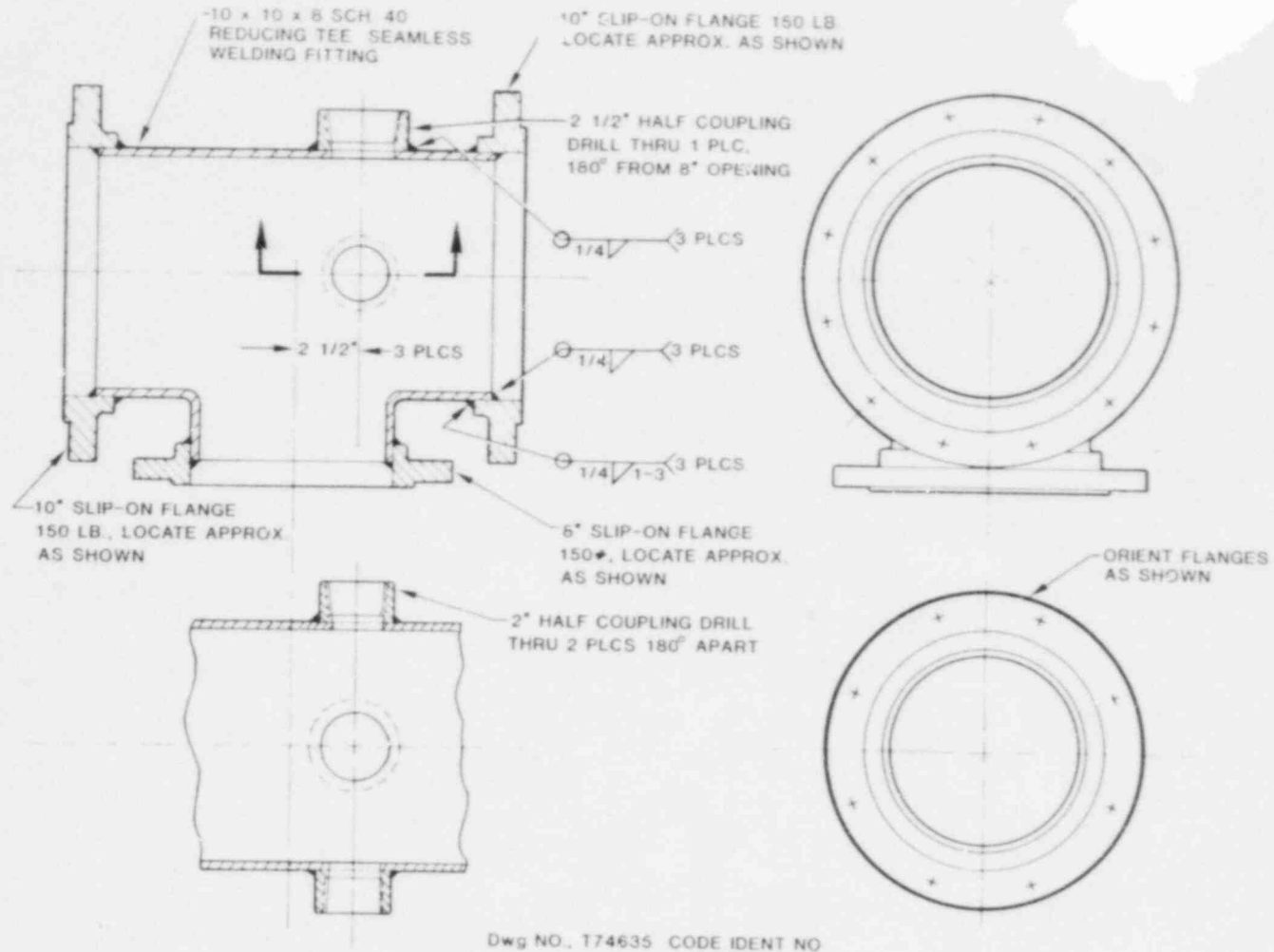


Figure 2-9. Sketch of chamber in which laser melted iron oxide drops will be dropped into water at ambient pressures up to 1.0 MPa. Chamber also can be used for controlled atmosphere studies at atmospheric pressure.

to 3 kg. FITS2A was conducted on April 19 and was intended to be a repeat of FITS1A with a larger melt mass and an adjusted entry velocity. An explosion was spontaneously triggered at the water surface-melt interface at 30 ms after melt entry. This explosion was as vigorous as in the exo-FITS series, but the entire melt mass was not submerged in the water prior to the explosion. The entry velocity was approximately 10% lower than a normal exo-FITS experiment.

Based on the observation from the first two in-chamber experiments, the melt entry velocity and shape appear to affect the spontaneous trigger. The melt entry velocities in exo-FITS, although not accurately measured (photometric data only), were nonetheless repeatable. Two subsequent exo-FITS experiments were performed in order to more accurately measure the entry velocity. Drops in chamber will have to be adjusted to achieve velocities in the range where spontaneous explosions occur. This work is in progress and should be done in time for FITS3A scheduled for mid June, 1980. Particle size data and data from active transducers were reduced for both FITS1A and 2A. Since no violent explosion occurred in 1A, active data were not obtained. However, particle size analysis was done for both experiments, and pressure data (chamber pressurization and temperature rise) were obtained for

FITS2A. Particle size distributions were significantly different for the non-exploding (FITS1A) experiment compared to FITS2A which exploded. In FITS1A, 96% of the particles were above 500- μm , while in FITS2A only 36.8% were above 500- μm with 25% less than 44 μm in average diameter.

The closure system in FITS2A vented prematurely and the long time chamber pressure (greater than 1 s) was not recorded. However, the two membrane pressure transducers (2kHz frequency response) recorded 0.75 bar and 0.55 bar peak pressures within 0.2 s after explosion. These pressure peaks are probably due to the explosion-driven airshock and debris. Data for times greater than 1 sec would be invalid due to the premature venting and the thermal response of these transducers. A temperature rise of 56°C in 1.8 s was recorded in the vessel.

Of the 2 exo-FITS experiments, MD-17 and MD-18, performed only MD-18 resulted in an explosion. Crucible vents were plugged in MD-17 and the melt was gassy resulting in a very dispersed non-uniform melt delivery. No spontaneous explosion resulted. MD-18 was very typical of past exo-FITS experiments and used a 3kg melt mass. The melt entry velocity was measured using photo-diode sensors and a propagating explosion was triggered at the

chamber base 146 ms after melt entry. The propagation velocity was found to be 313 m/s. Other data from pressure transducers in the water chamber are now being reduced.

2.3.1 FITS Experiments

FITS2A

The second in-chamber experiment was conducted on April 19, 1980. The melt delivery velocity was adjusted to attempt to reproduce the velocities obtained in exo-FITS, and the melt mass was increased to 3 kg. As reported earlier 2 kg masses are near the threshold for spontaneous explosions for the conditions and materials used in these experiments. Table 2-II describes the parameters for this experiment.

TABLE 2-II

FITS2A Parameters

Melt:	3.0 kg Fe/Al ₂ O ₃ Thermite
Coolant:	152.0 kg water at 13°C; 533 mm deep
Chamber:	Lucite 610 mm sq x 533 mm deep; 3.18 mm thickness
Pressure:	0.83 bar
Melt entry velocity:	4.6 m/s

This experiment resulted in an explosion, spontaneously triggered at the melt-water surface interface 30 ms after melt entry. The explosion was as violent as those seen in exo-FITS experiments but the entire melt mass was not submerged in the water at the time of the explosion. The melt entry

velocity was approximately 10% lower than desired which may have contributed to the difference in triggering behavior. The melt entry velocity and perhaps shape appear to have some effect on the probability and location of triggering. Work is in progress to understand this behavior in FITS.

The chamber vented prematurely; therefore, meaningful chamber pressure rise data for times greater than one second were not obtained. The membrane pressure transducers, intended to study chamber pressurization, yielded data related to the pressure spike due to the explosion driven air shock and debris. Data from those transducers is also limited to 2 s due to the thermal response of these devices. Figures 2-10 and 2-11 describe the pressures observed. The transducers are located 1.6 meters apart in the chamber and the differences in wave shape were expected.

A temperature rise of 56°C in 1.8 s was also recorded during this experiment.

2.3.2 FITS Particle Size data

Debris from FITS1A and FITS2A were analysed for particle size distribution using standard sieving techniques. The sieve sizes used are described in Table 2-III and plots of weight percent versus average diameter are shown in Figure 2-12.

R80176500 P6 FITS2A

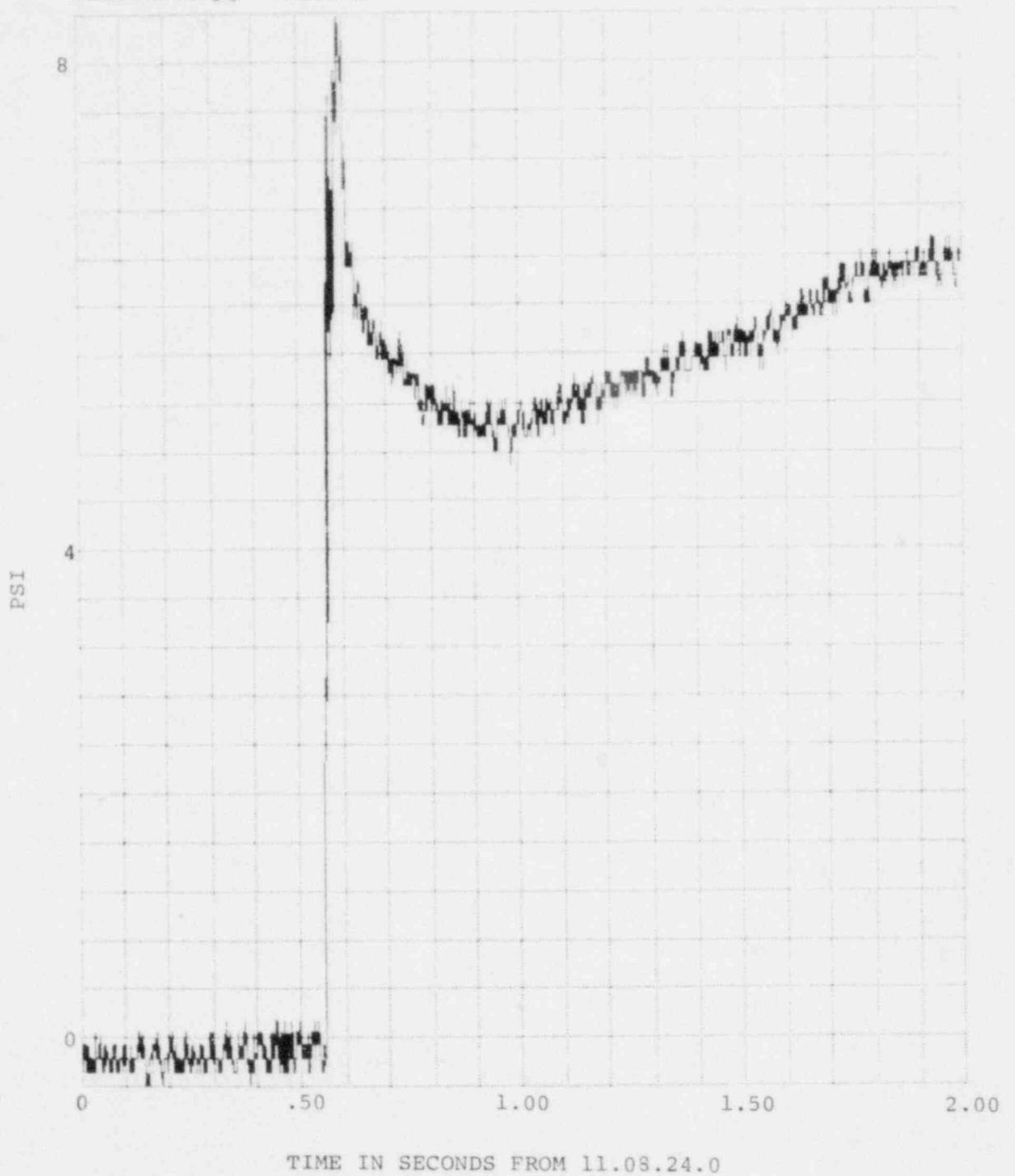


Figure 2-10. Transient Pressure in FITS Chamber for FITS2A (Pressure Transducer P6)

R80176500 P7 FITS2A

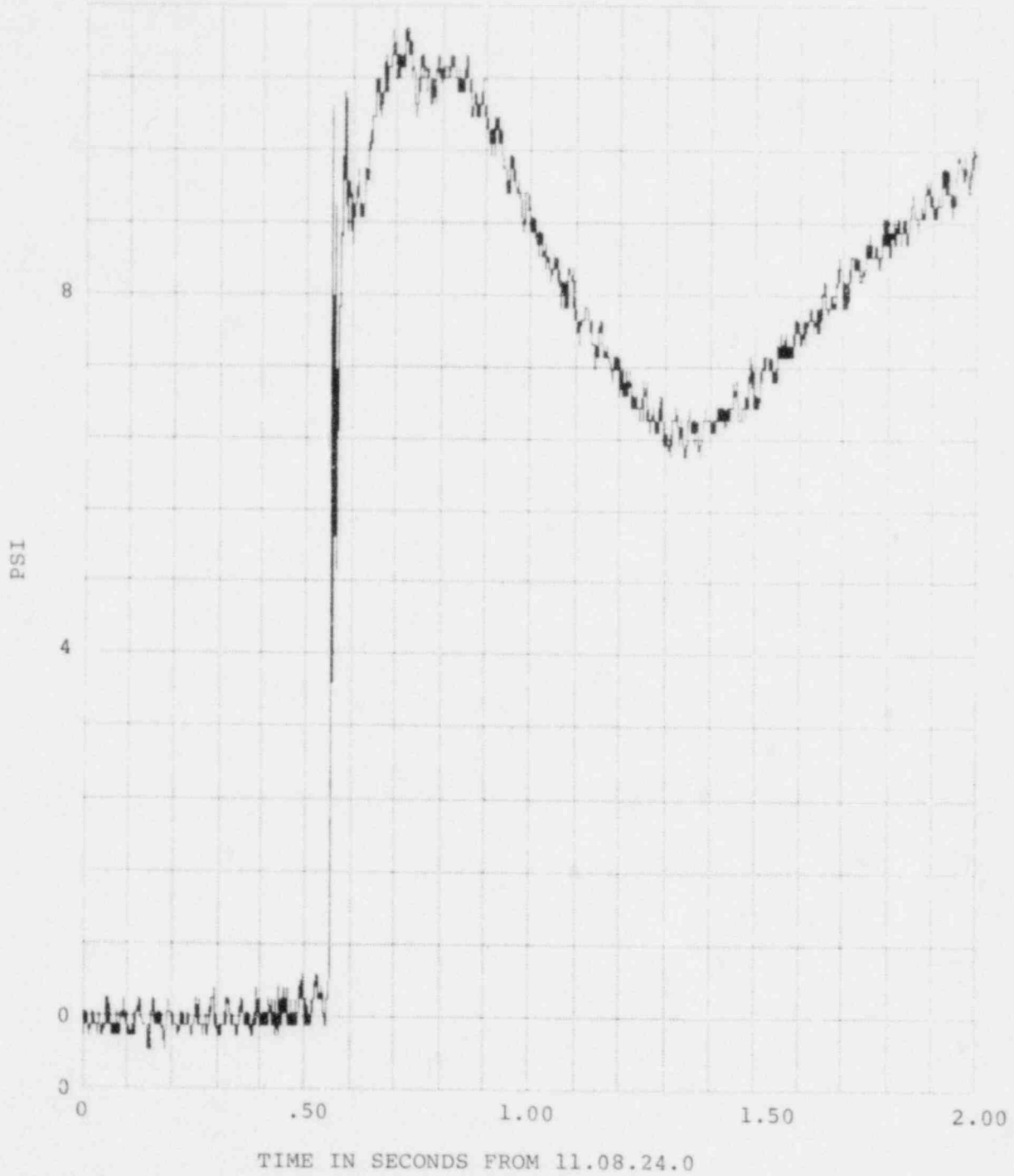


Figure 2-11. Transient Pressure in FITS Chamber for FITS2A (Pressure Transducer P7)

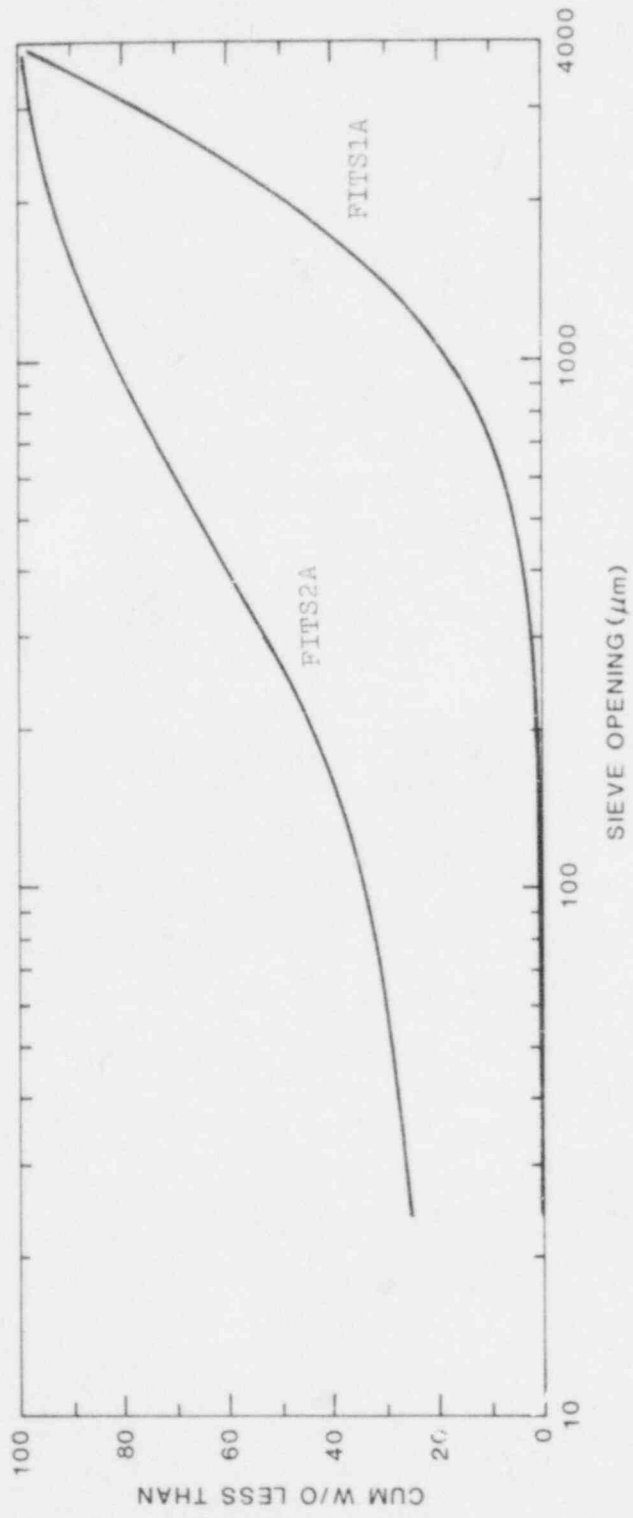


Figure 2-12. Particle Sieve Size Data (FITS1A and FITS2A)

TABLE 2-III
Sieve Characteristics

Fraction Sizes in mm

<u>Maximum</u>	<u>Minimum</u>	<u>Average</u>
----	2000	4000*
2000	1000	1500
1000	840	920
840	500	670
500	351	426
351	246	298
246	177	212
177	149	163
149	105	127
105	74	90
74	44	59
44	--	22

* Assumed for plotting

Figures 2-13 and 2-14 show portions of the debris from these two experiments and further indicate the differences between the two. Most of the debris is spherical in nature and some of the larger particles (> 10 mm) are essentially hollow spheres. Further analysis of this debris is planned.

2.3.3 MD-Series EXO-FITS Experiments

Two additional exo-fits experiments were conducted to better measure melt entry velocity and to study the effect of this initial condition in explosivity so that better control can be obtained in the FITS experiments. It was not felt originally that explosivity and triggering

POOR ORIGINAL

FITSIA
DEBRIS > 500 μ m
96% OF TOTAL



Figure 2-13. Fuel Debris for Particle Sizes Greater than 500 μ m for FITSIA

POOR ORIGINAL

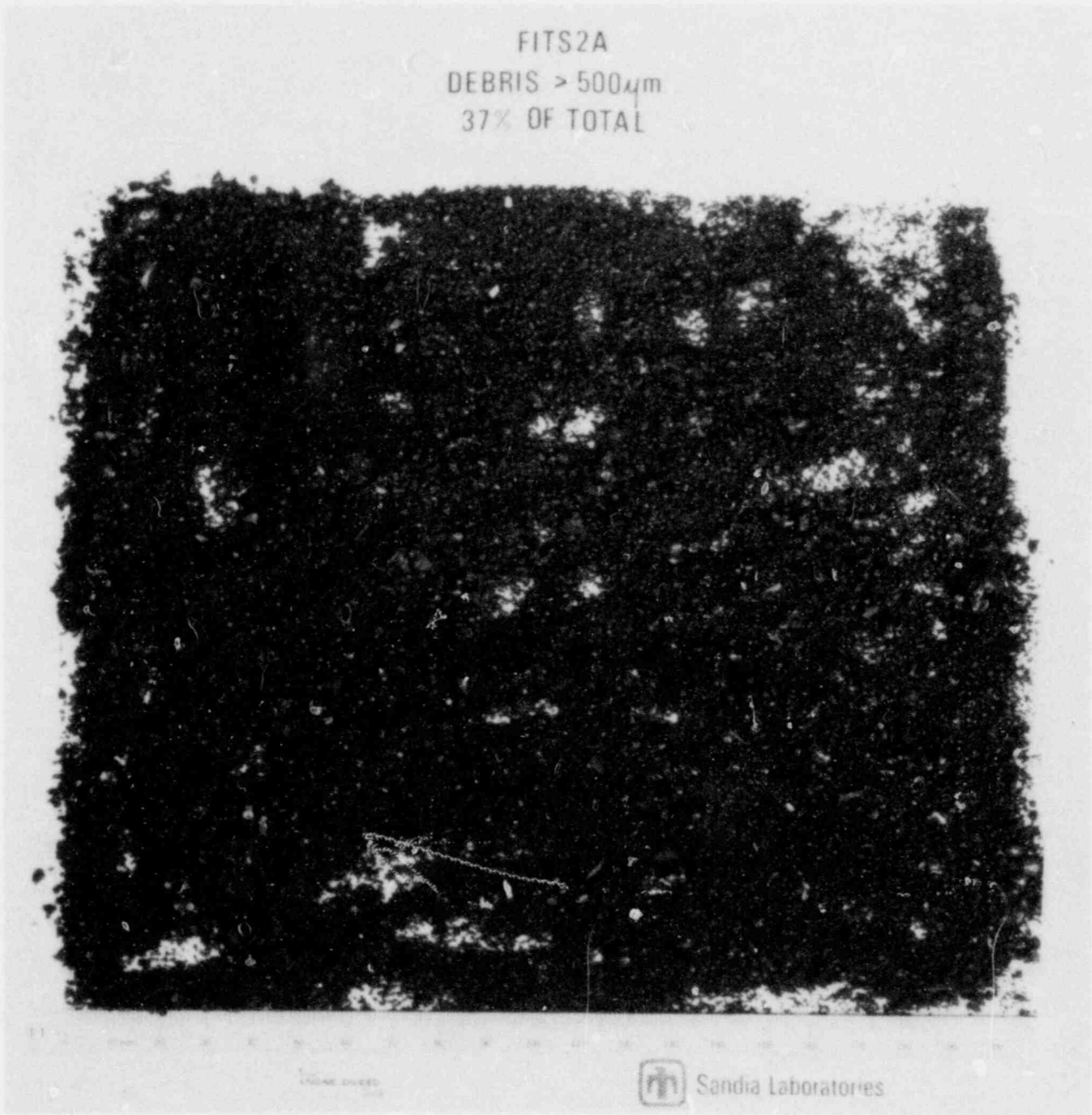


Figure 2-14. Fuel Debris for Particle Sizes Greater than 500 μ m for FITS2A

location would be as sensitive to melt entry parameters as they appear to be.

Experiment MD-17 was not successful since crucible vents apparently were plugged during the thermite burn and resulted in a very gassy dispersed, non-uniform delivery.

MD-18 was a successful experiment in which a 3 kg mass was used. Melt entry velocity was obtained using photo-diode melt sensors and data from lithium niobate and quartz pressure transducers were obtained. Those data are still being reduced. Table 2-IV highlights the results and initial conditions of experiment MD-18.

TABLE 2-IV

MD-18 description

Melt: 3.0 kg (2.74 kg delivered)

Water: 152 kg at 19.5c, 533 mm deep

Chamber: Lucite, 610 sq x 533 deep x 4.76 mm thick wall:
3.18 mm thick base

Melt entry velocity: 4.62 m/s

Time to explosion from melt entry: 0.146 sec

Propagation vel: 313 ± 20 m/s

Melt average dia: 30 cm

Melt apparent density at explosion: 0.108 gm/cm^3

2.4 Modelling and Analysis of Steam Explosions

2.4.1 Core Disruption and Meltdown Accident Progression

A major area of uncertainty in the core meltdown scenario for the LWR is how the geometry of the core is initially disrupted and how the meltdown progresses. It is known that a number of physical processes may challenge containment integrity during or following a meltdown, e.g. hydrogen combustion, molten-core-concrete interactions, steam explosions. However, many of the details of disrupted core behavior or core material motion are not well understood^{5,6}, e.g.,

- (1) Thermal hydraulics in a severely damaged core
- (2) Material motion during melting
- (3) Heat transfer to surrounding structure from a molten core
- (4) Vessel failure and subsequent heat transfer in containment

Consider a failure and the subsequent heat transfer in the containment. Past attempts to model these events used the core meltdown computer model MARCH⁷. From the MARCH analysis it was determined that the molten material would fail the lower plenum and fall into the reactor cavity below. The containment pressure would rise over the next few minutes because of the steam released from the primary system and the steam subsequently

produced in the reactor cavity by boiloff of the residual water and water from the accumulators. Pressure would decrease later as condensation on cold walls would begin to take effect.

For example Figure 2-15 illustrates this behavior for the TMLB' accident sequence where the reactor trips and all electrical power is lost at the plant site. The peak in pressure occurs because the rate of water boiloff is initially much larger than the rate of condensation on the walls. This behavior could threaten the containment integrity by overpressure early in the accident scenario.

The calculated magnitude of this steam pressure "spike" depends on the models used to describe the rate of water boiloff and steam condensation as the core is quenched in the reactor cavity. MARCH models assume that the molten core catastrophically fails the lower plenum of the vessel, falls into the reactor cavity with water and instantaneously fragments into small particles in the water pool (Figure 2-16). The core then heats up the water to saturation and begins boiling it away. This scenario although self-consistent may not be realistic. Rivard et al in Chapter VI of the ZIP Study⁶ suggested that the vessel may fail locally rather than catastrophically causing the molten core to fall more slowly into the cavity (Figure 2-17). If the plenum did fail catastrophically

PRESSURE IN CONTAINMENT VOLUME NO. 1, PSIA

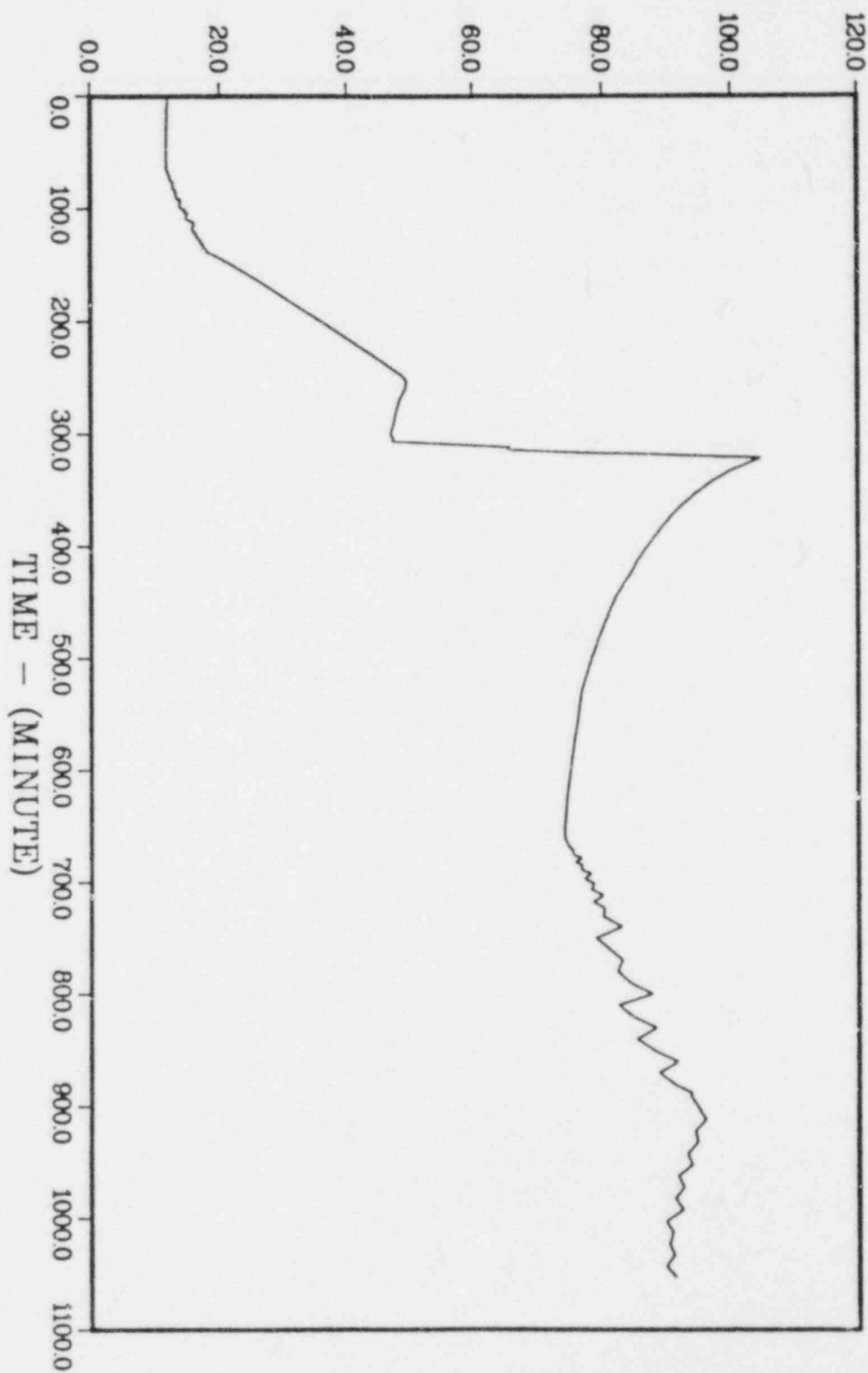


Figure 2-15. Pressure in Containment, in PT 3 TMLB'

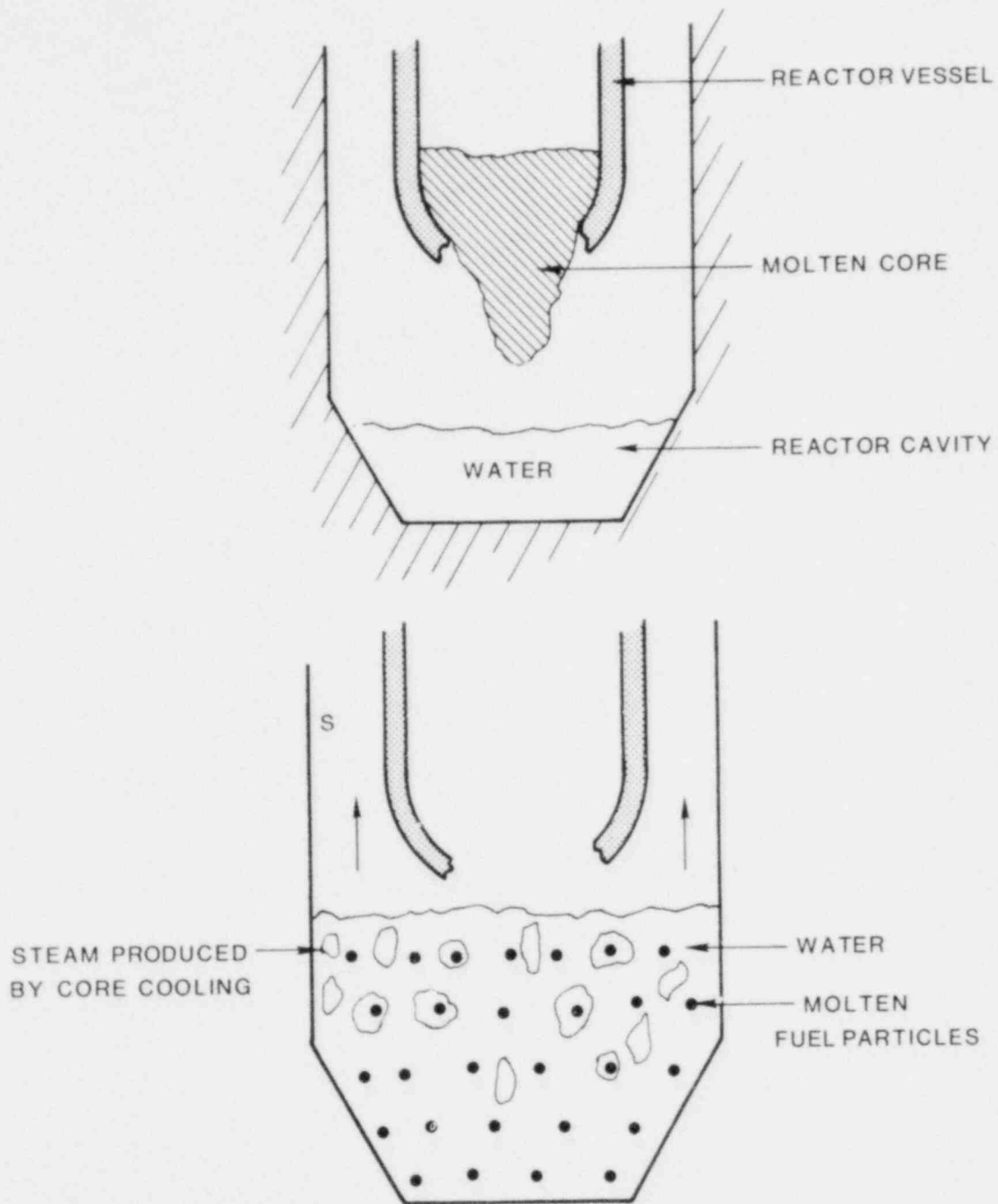


Figure 2-16. Conceptual Picture of MARCH Model for Core Quenching

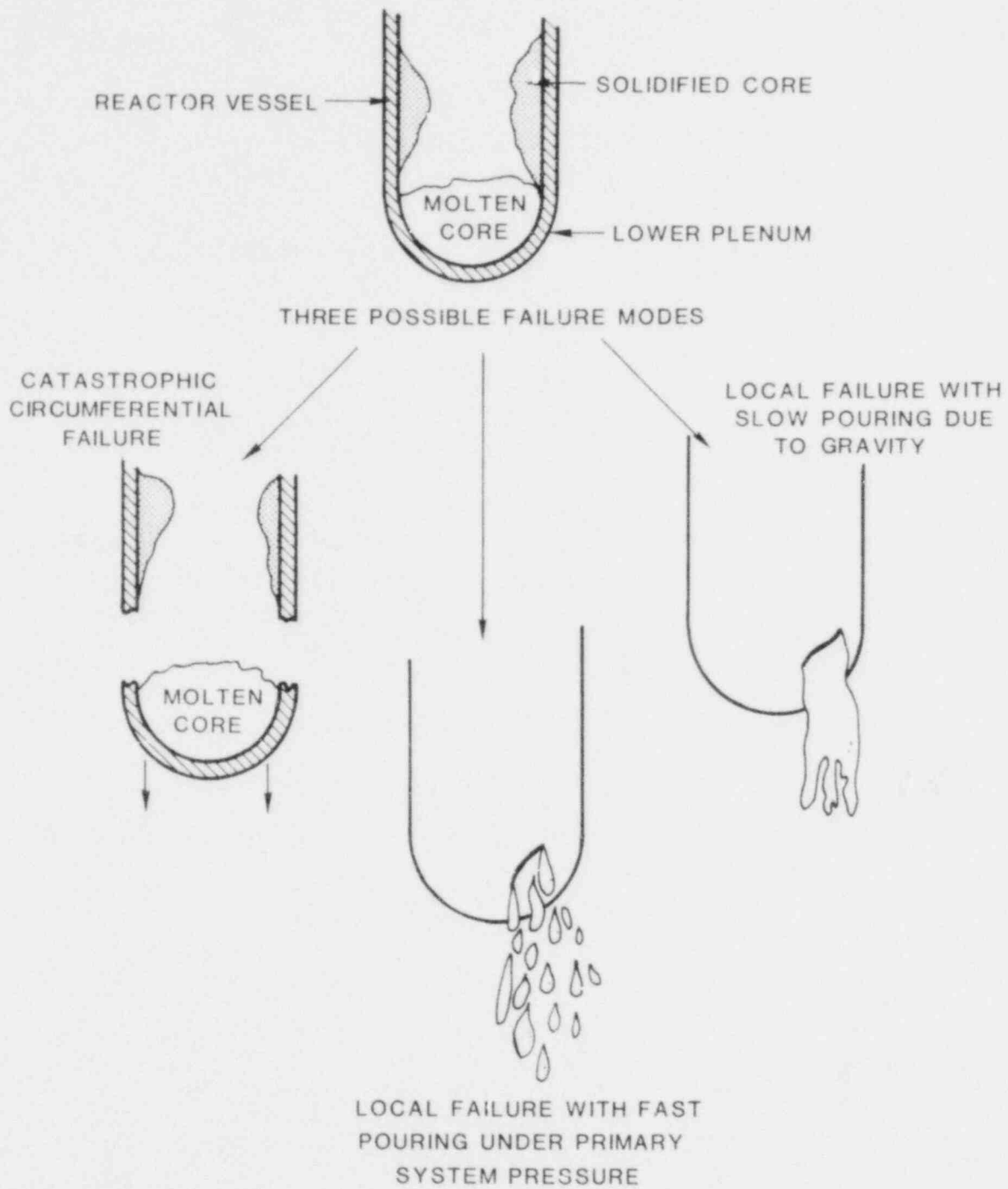


Figure 2-17. Various Possible Modes of Lower Plenum Failure

the core would enter the water not as particles but as a large volume ($D \sim 2-3$ m).

The extent of fuel breakup during this fall for either case is uncertain. From experimental observations of the exo-FITS and in-vessel FITS tests it appears that a melt introduction into water by pouring can fragment the fuel into small particles ($\sim 10-20$ mm) in a short time (< 1 sec). However at much larger scales, as in the reactor situation, it is not known if this particle size range would be achievable.

Once the molten fuel settles onto the reactor cavity there are four ways by which the melt could be quenched (Figure 2-18).

- (i) The melt falls into a dry cavity and the accumulator water falls on top of the melt.
- (ii) The core melt becomes a fluidized bed in the water with particles initially in film boiling.
- (iii) The core melt falls into the water and settles as a debris bed.
- (iv) The core melt falls into the water and a steam explosion occurs.

A fluidized bed is defined as a particle bed which remains dispersed and suspended in the water-steam continuum due to the high steam flowrate out of the bed caused by water vaporization. A debris bed is defined as a stationary particle bed which settles due to gravity on

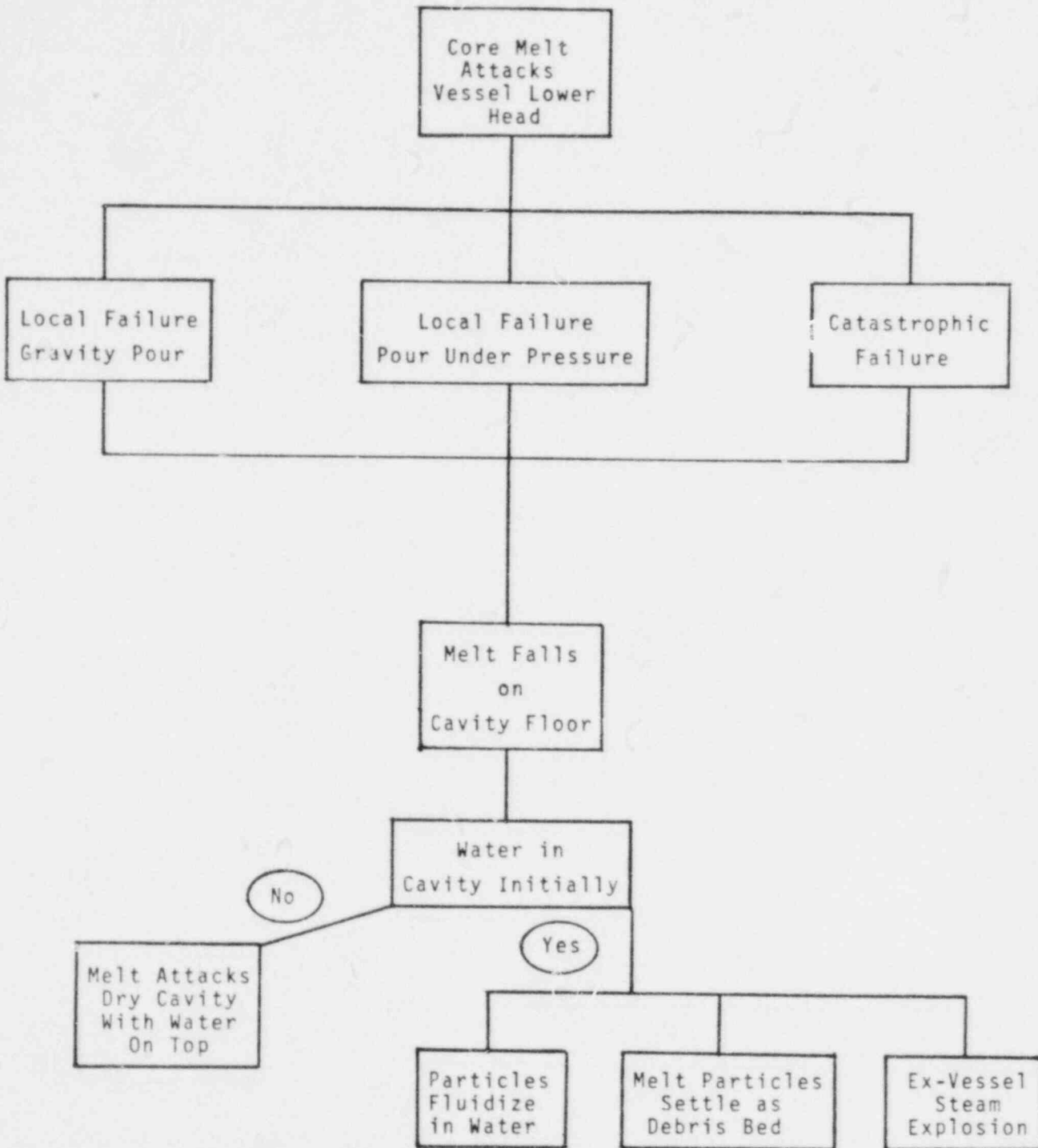


Figure 2-18. Block Diagram of the Possible Scenarios for Molten Core Entry into the REactor Cavity

the cavity floor and contains a water-steam mixture in the interstices between the fuel particles.

Let us now examine the effect on the containment pressure.

The first possibility would produce steam by boiling away the overlying water above the core melt as a molten-core-concrete interaction begins. The maximum rate of steam production is limited by the critical heat flux in pool boiling, and this value ($\sim 10^6$ W/m²) would lower the steam production rate from the MARCH value such that the peak overpressure of the containment would be lower ($\sim 70\%$ of peak value), because of steam condensation, for TMLB'.

The second scenario, although physically possible, was shown to be unrealistic for full scale reactor conditions by Rivard⁸ for fuel particles larger than 1-2 mm. This particle size appears to be a lower bound value for the case of no explosion. Thus the particles would not likely fluidize but would settle as a debris bed.

Formation of a debris bed would also limit the rate of steam production and pressure buildup because liquid water must penetrate the bed from above as steam flows out. The maximum rate of steam production is limited by the bed dryout heat flux. By using the dryout model proposed by Lipinski⁹ an analysis of the peak pressure in containment considering a debris bed was carried out. Figure 2-19 illustrates some sample results for the Surry reactor

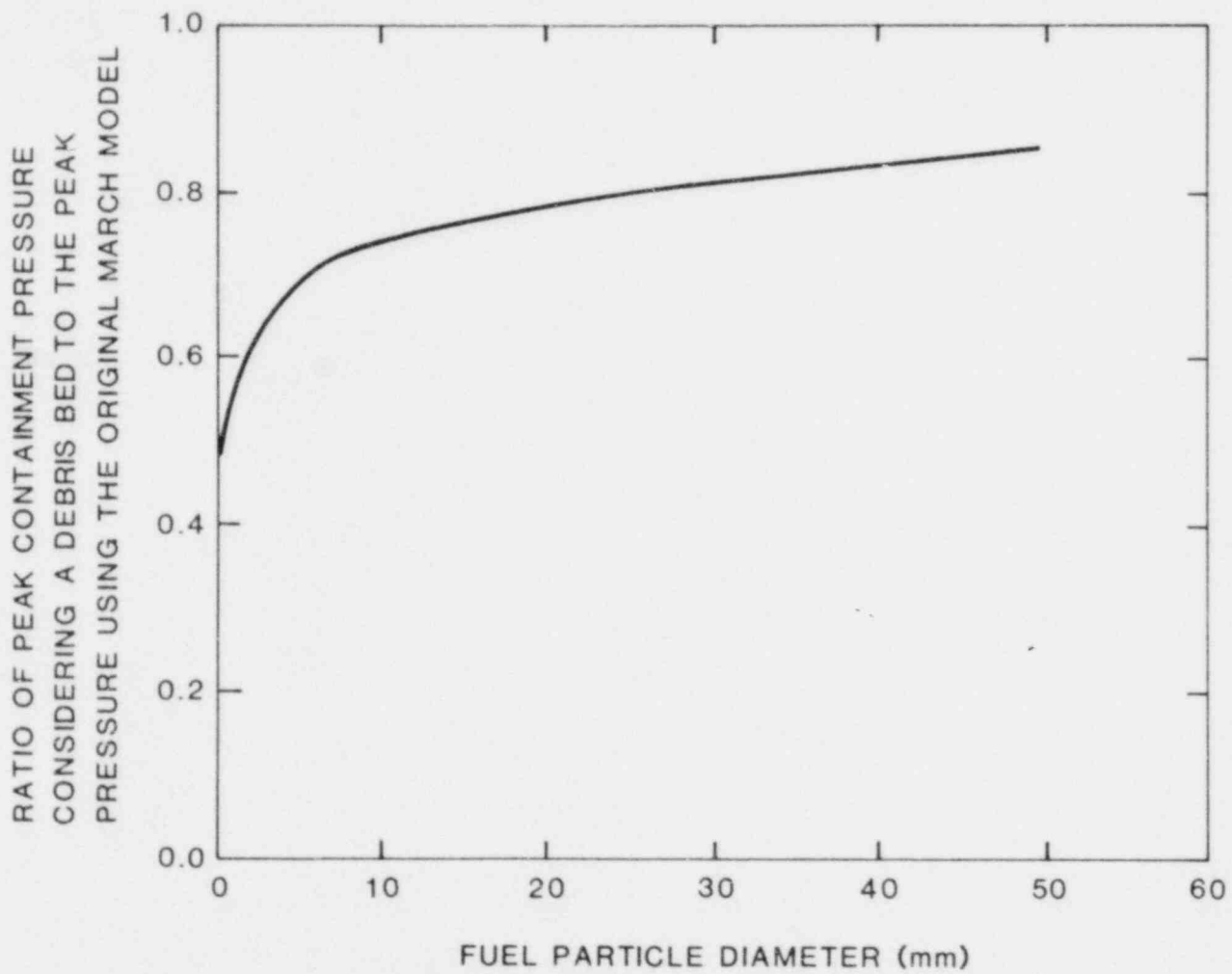


Figure 2-19. Debris Bed Limiting Steam Pressurization
 Surry Reactor - TMLB Accident

for the TMLB' accident sequence. These results indicate that a debris bed could also significantly limit the peak pressure in containment due to water boiloff in the reactor cavity.

The final possibility of an ex-vessel steam explosion is much more difficult to analyze. It is expected that the explosion would not threaten the containment directly (e.g., the static overpressure in containment due to the explosion would be at most ~ 0.1 MPa); but it would disperse and fragment the hot molten core. This may have either of two effects. If the core debris is in large fragments and is dispersed into subcooled water then further rapid containment pressurization would be minimal.

If the core debris is in small fragments and is dispersed in saturated water and/or air more steam production and direct atmospheric heating are possible and this would raise the containment pressure further.

The pressure rise time would be of the order of a few minutes. Work is continuing in this area and future small scale and FITS experiments are expected to aid in the understanding of fuel fragmentation from the explosion.

2.4.2 One-Dimensional Transient Explosion-Propagation Model

Once the trigger induces film collapse the rapid heat transfer process begins. This induces a local pressure

increase, and a collapse of nearby vapor films. The resulting effect propagates through the mixture. There is extensive research work involved in this phase of explosion; however, at present relatively little is known about how the explosion propagates, or the detailed mechanisms for fuel fragmentation and fuel-coolant heat transfer.

To mechanistically model the propagation phase of the fuel-coolant interaction in large scale systems, we have developed a transient one-dimensional computer model, based upon a two-phase flow theory. The model represents the mixture as an array of molten fuel drops, each surrounded by a vapor film immersed in the liquid coolant. A more detailed description is presented in the previous quarterly⁵ and a topical report is being prepared to describe the models in detail.

This quarter a parametric study was done to determine the effect of changing the trigger magnitude and fuel-coolant volume fractions. The initial conditions are given in Table 2-V and the explosion propagation velocity is also given as one result of the analysis. A thermal mechanism for fuel fragmentation was used in these calculations; this mechanism is based on the concept that film collapse causes liquid-liquid contact and rapid vapor production fragments the fuel due to Taylor instabilities.

TABLE 2-V

Parametric Study of a One-Dimensional Steam Explosion

Case Number	Trigger Magnitude $P_p - P^\infty$ (MPa)	Fuel Drop* Diameter D_F (m)	Initial Steam Film Thickness δ_V (mm)	Initial Fuel Volume Fraction** α_F	Initial Steam Volume Fraction*** α_V	Explosion Propagation Velocity V_D (m/s)
1	10	0.01	0.6	0.035	0.015	1000
2	3	0.01	0.6	0.035	0.015	750
3	1	0.01	0.6	0.035	0.015	No propagation
4	10	0.02	0.6	0.27	0.015	900
5	10	0.01	2.0	0.035	0.08	350
6	10	0.01	6.0	0.035	0.45	100

* Initial Fuel Temperature (T_F) = 2300 K. Initial Coolant Temperature (T_C) = 300 K.

** Thermal Fuel Fragmentation Mechanism -

$$\alpha_F = \frac{\frac{\pi}{6} D_F^3}{\text{Unit Cell Volume}}$$

*** Thermal Fuel Fragmentation Mechanism -

$$\alpha_V = \frac{\frac{\pi}{6} [(D_F + \delta_V)^3 - D_F^3]}{\text{Unit Cell Volume}}$$

The transient propagation of the explosion is illustrated in Figures 2-20 and 2-21 for two sets of initial conditions; one with a small fuel volume fraction characteristic of the FITS tests (Figure 2-20) and the other with a much larger fuel fraction (Figure 2-21). The pressure profile of the explosion is shown at two different points in time. Notice that the peak pressure grows in time in both cases, with the peak pressure at the later times representative of the steady-state propagation value. The profile initially rises quite sharply in both cases as the film is predicted to collapse and rapid fuel fragmentation begins. As vapor is produced and expands against the surrounding liquid the pressure decreases to ~10-20 MPa about 0.2-0.4 m behind the propagation front. The difference in fuel volume fraction has two effects; it causes the peak pressures to be higher and it slows the explosion propagation (Table 2-V). The first effect is due to the increased rate of thermal energy being deposited in the fuel in a given time span. The second effect is qualitatively observed in the FITS experiments⁵.

When the initial steam volume fraction is increased or the trigger pressure is decreased the explosion propagation is slowed. In the first case the compliance of the multiphase system is increased and thus it takes longer for the pressure signals from the explosion to be transmitted to neighboring fuel drops, cause collapse and

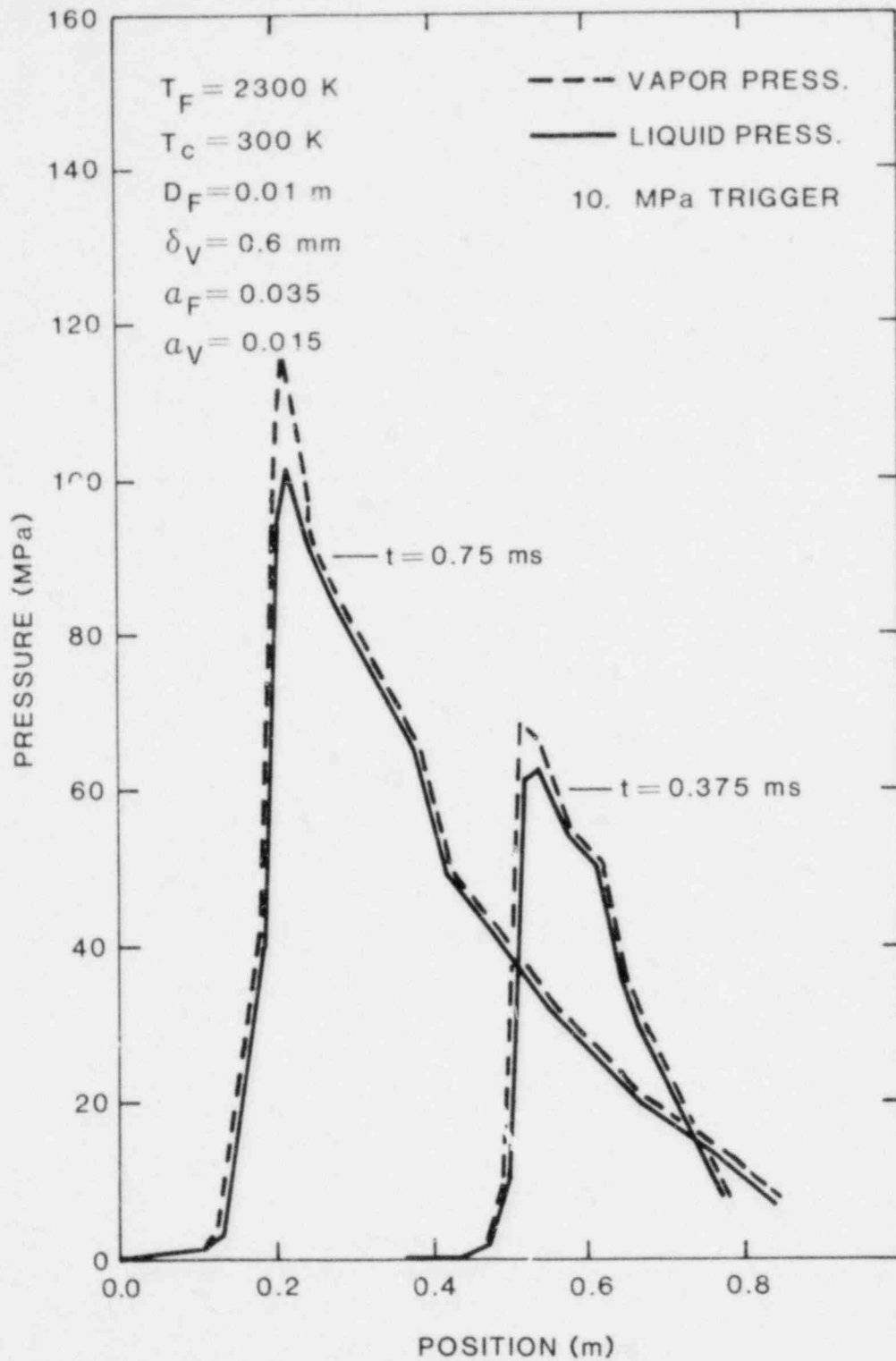


Figure 2-20. One-Dimensional Explosion Calculation Using a Thermal Fuel Fragmentation Mechanism for $a_F = 3.5\%$

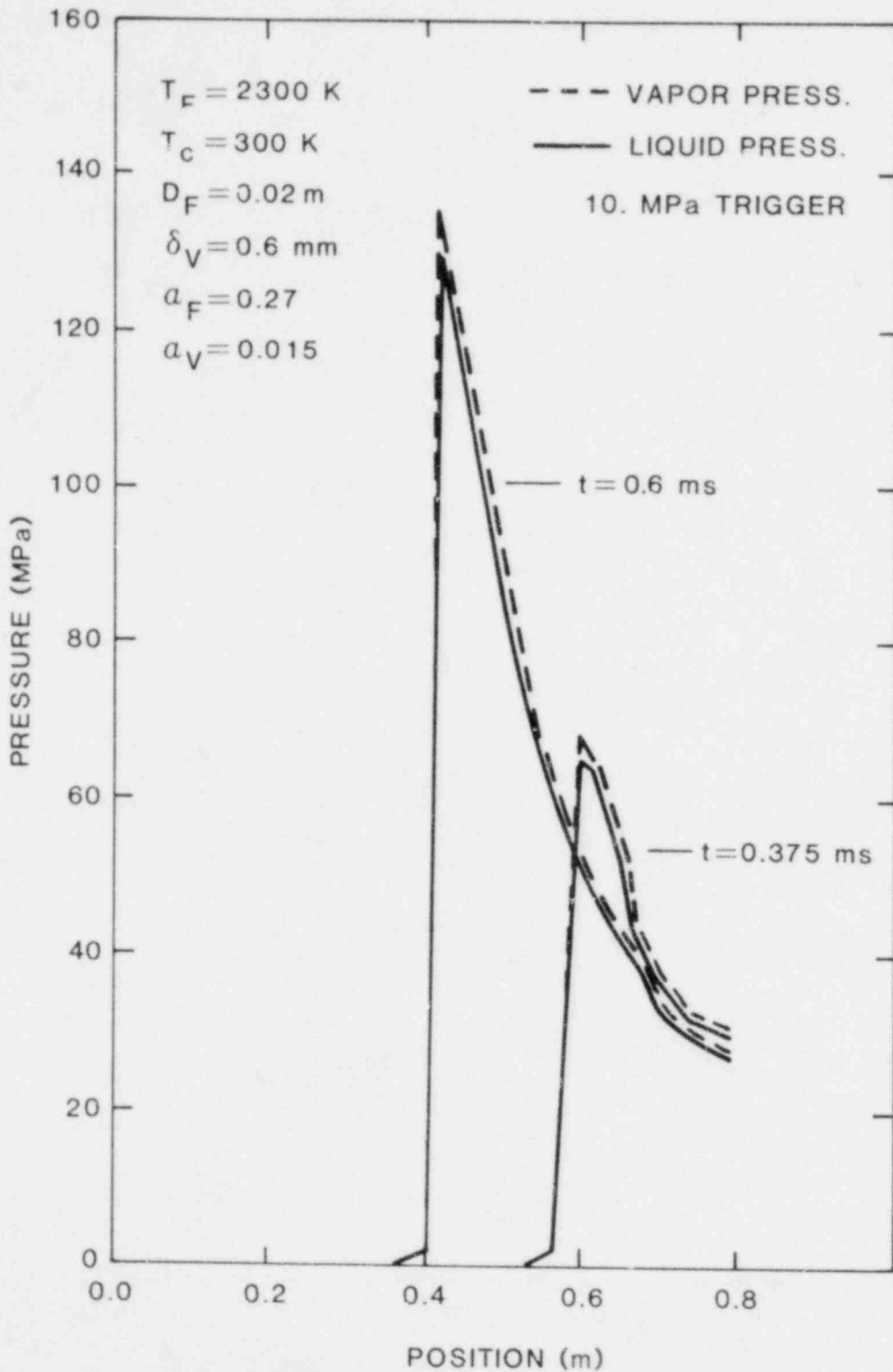


Figure 2-21. One-Dimensional Explosion Calculation Using a Thermal Fuel Fragmentation Mechanism for $\alpha_F = 27\%$

propagate the explosion. In the second case the initial and subsequent collapses are slowed in time when the trigger pressure is reduced.

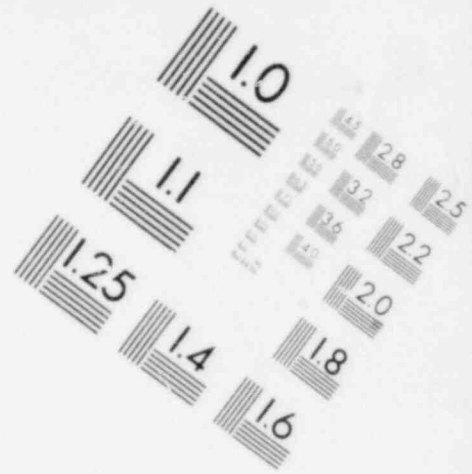
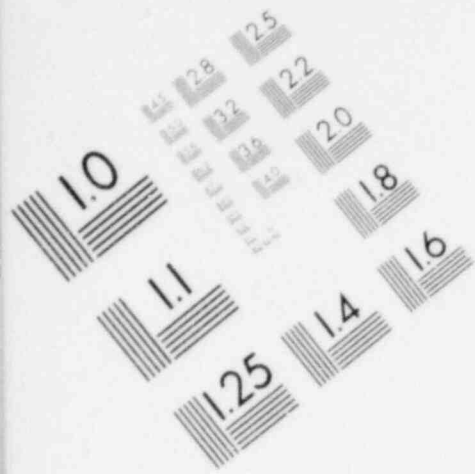
Future work will consist of including other fuel fragmentation mechanisms in the model, improving existing models, and attempting to analyze the FITS test results.

2.4.3 Empirical Explosion Modelling

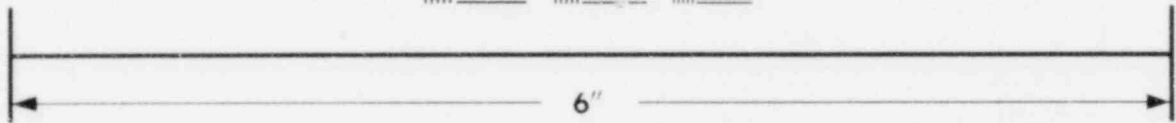
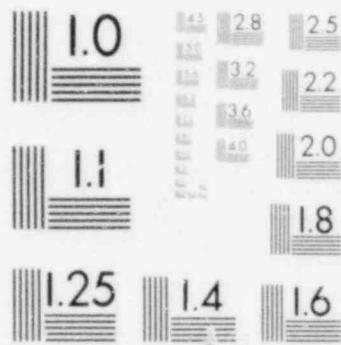
We began work this quarter on empirically describing the steam explosion by developing a two-dimensional hydrodynamics model. The purpose of this effort is to link the experimental results from FITS and more detailed mechanistic analysis to the fluid-structural calculations by an empirical explosion model. This method is very useful because only major inputs are needed from experiments on other analysis; e.g.

- (i) a consistent equation of state for water,
- (ii) thermal energy deposition rate to the water from the fuel,
- (iii) the propagation velocity of the explosion as a function of the initial conditions.

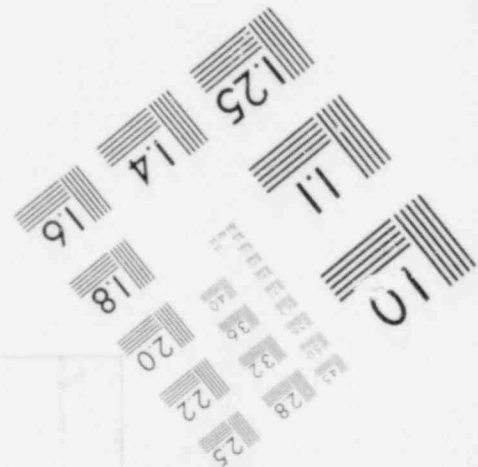
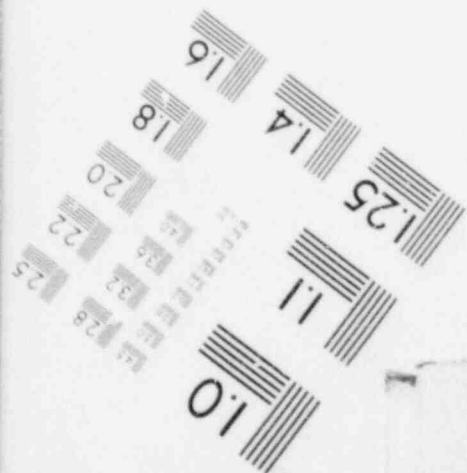
This quarter an approximate equation of state for water was developed using the analytic equation of state expression developed for the Sandia hydrodynamic codes¹⁰. The equation of state, although approximate, will be quite useful in this model because it is consistent over a much larger temperature and pressure range than the



**IMAGE EVALUATION
TEST TARGET (MT-3)**



MICROCOPY RESOLUTION TEST CHART



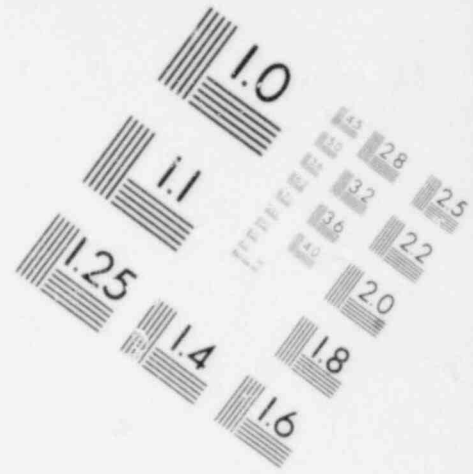
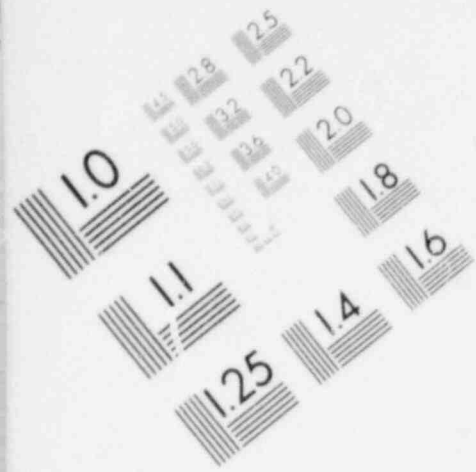
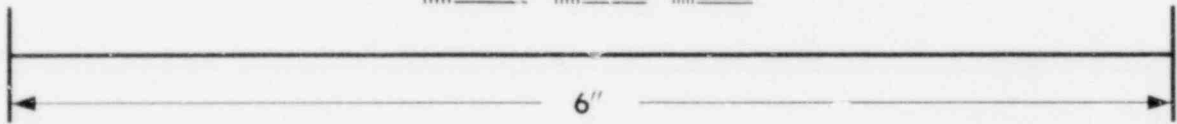
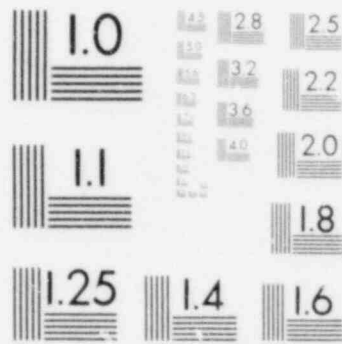
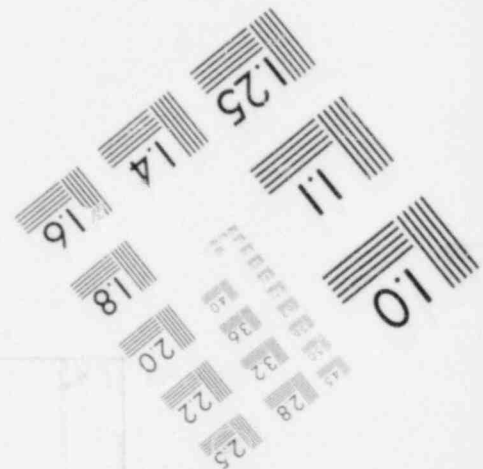
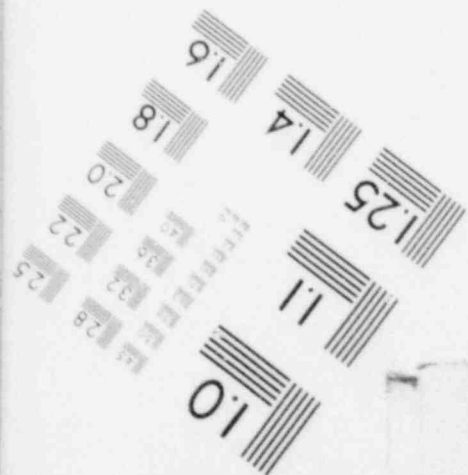


**IMAGE EVALUATION
TEST TARGET (MT-3)**



MICROCOPY RESOLUTION TEST CHART



ASME steam tables. Next quarter some sample calculations using the model will be done.

2.5 Structural Consequences of the Steam Explosion

During this quarter the calculations performed for the Zion-Indian Point Study were reviewed and the writing of the second topical report on containment failure was begun.

2.6 References

- ¹M. A. Maurakh, B. C. Mitin, and M. B. Roitber, "Contactless Measurement of the Density and Surface Tension of Liquid Oxides at High Temperatures," Zavodsk. Lab. 33 (8), 984 (1967).
- ²Handbook of Chemistry and Physics, 56th Edition, R. C. Weast, Ed., CRC Press, Cleveland, Ohio, April 1975.
- ³H. Mizuta, "Fragmentation of Uranium Dioxide after Molten Uranium Dioxide-Sodium Interaction," J. Nucl. Sci. Tech. 11 (11), 480 (1974).
- ⁴L. S. Nelson, L. D. Buxton, and H. N. Planner, Steam Explosion Triggering Phenomena. Part 2: Corium-A and Corium-E Simulants and Oxides of Iron and Cobalt Studied with a Floodable Arc Melting Apparatus, SAND79-0260, Sandia National Laboratories, Albuquerque, New Mexico, May 1980.
- ⁵Light Water Reactor Safety Research Quarterly Reports, M. Berman, Editor and Person in Charge, Sandia National Laboratories, Albuquerque, New Mexico -
July - September 1979, SAND79-2290, June 1980
October - December 1979, SAND80-0927, July 1980
January - March 1980, SAND80-1304/lof4, August 1980
- ⁶Report of the Zion/Indian Point Study: Vol. I, SAND80-0617/1, W. B. Murfin, Compiler, Sandia National Laboratories, Albuquerque, New Mexico, NUREG/CR-1410, June 1980.
- ⁷R. O. Wooton, and H. I. Avci, MARCH Users Manual, Battelle Columbus Laboratories, Columbus, Ohio, January 1980.

- ⁸J. Rivard, Sandia National Laboratories, Private Communication, May 1980.
- ⁹R. Lipinski, Sandia National Laboratories, Private Communication, May 1980.
- ¹⁰S. L. Thompson, CKEOS2 - An Equation of State Test Program for the Chart D/CSQ EOS Package, SAND76-0175, Sandia National Laboratories, Albuquerque, New Mexico, May 1976.

3. Separate Effects Tests for TRAP Code Development (J. C. Cummings, R. A. Sallach, R. M. Elrick)

3.1. Introduction

The purpose of this program is to investigate experimentally the chemistry of fission products in the primary system of light water reactors during various accidents involving fuel-rod rupture and/or melting. Specifically, the program is to provide experimental data to be used for input to the TRAP code, which describes the transport and deposition of fission products during such accidents. The need for such a program is based on the considerable uncertainty that exists as to the chemical compounds that form and their basic properties.

The major portion of the effort in the program involves laboratory-scale experiments to investigate:

- vapor pressures of fission-product species at elevated temperatures (Knudsen-effusion and transpiration tests), and
- chemical compound formation and reaction rates for multiple fission-product species in high-temperature-steam environments (Laser Raman Spectroscopy tests).

Principal fission-product species to be investigated include, in order of priority, compounds of non-radioactive cesium, iodine, strontium, tellurium, and possibly rubidium, selenium, and ruthenium. The program also includes analytical studies to evaluate related research and to assist in the development of the TRAP code.

3.2. Progress

The major purpose of these separate-effects tests is to provide information and data needed by the TRAP code. The required information concerns the vapor species containing fission-product elements which can coexist in high temperature steam. Typical input data for the TRAP code are the vapor pressure of the source compounds for these vapor species and the kinetics of their interaction with each other and with vessel materials.

A dual approach is being used to attain the program goals. First, there are chemical experiments in which vapor pressure and kinetic data are obtained. Second, a Fission Product Reaction Facility is being constructed in which laser Raman spectroscopy will identify or verify the vapor species and investigate vapor-vapor interactions. These are discussed in the following paragraphs.

A contract was awarded to the New Mexico Institute of Technology for the determination of the vapor pressure of cesium hydroxide (CsOH). To date, the output of data has been low and the precision poor. Consequently, this contract has been cancelled and the work transferred to Sandia. The data which have been obtained are semi-quantitative in nature: (1) the vapor pressure of CsOH is comparable to CsI; and (2) there are indications that the vaporization of CsOH is enhanced by the presence of water vapor.

The dissociation of tellurides formed on nickel and stainless steel surfaces has been investigated through a series of scoping experiments. Samples containing ~ 100 g Te/mm² were heated to various temperatures in various gaseous flow environments. No dissociation of tellurium was observed until the temperature reached 850°C in either dry or wet flowing nitrogen (wet means saturated with water at room temperature). With wet nitrogen the reaction



is possible. The effluent gas was bubbled through an alkaline solution; however no Te⁼ ion was found indicating that the above reaction is not significant.

When hydrogen was added to the gas stream, evolution of tellurium vapor began at 750°C. No H₂Te was found. This behavior cannot be explained by thermodynamic arguments if one assumes the dissociation of metal tellurides. The result may indicate that mixed metal-oxides-tellurides are being decomposed; further study is needed.

Lower limits to the dissociation pressure of the metal tellurides can be calculated from the parameters of the experiments provided that all the tellurium has vaporized. This occurred when a nickel telluride surface was heated to 930°C. The surface coverage of tellurium (a total of 50 mg Te) was vaporized within 100 minutes, thus the rate of evaporation

or dissociation is at least 2×10^{-6} moles Te_2/min . During the experiment, the N_2 flow was 0.15 liter/min or 5.3×10^{-3} moles N_2/min . If equilibration of the gas by Te_2 vapor is assumed to occur, then the partial pressure of Te_2 (dissociation pressure of nickel telluride) is $\sim (2 \times 10^{-6} / 5.3 \times 10^{-3}) \times 650 \text{ torr} = .25 \text{ torr}$. This is a lower bound, any other assumption gives greater values.

3.3. Fission Product Reaction Facility

Detailed design of the facility has been completed with the exception of the Raman cell for which conceptual design drawings have been made. Final design of the cell will await testing of the interim Raman cell.

Fabrication has been completed on all major elements shown in Figure 3-1 with the exception of the Raman cell. Also fabricated were adjustable tables for positioning the facility with respect to the Raman spectrometer.

Essentially, all remaining purchased items are scheduled for delivery by the end of July at which time final assembly and checkout of the system will begin. The completed system, including the Raman cell, should be validated during the next quarter.

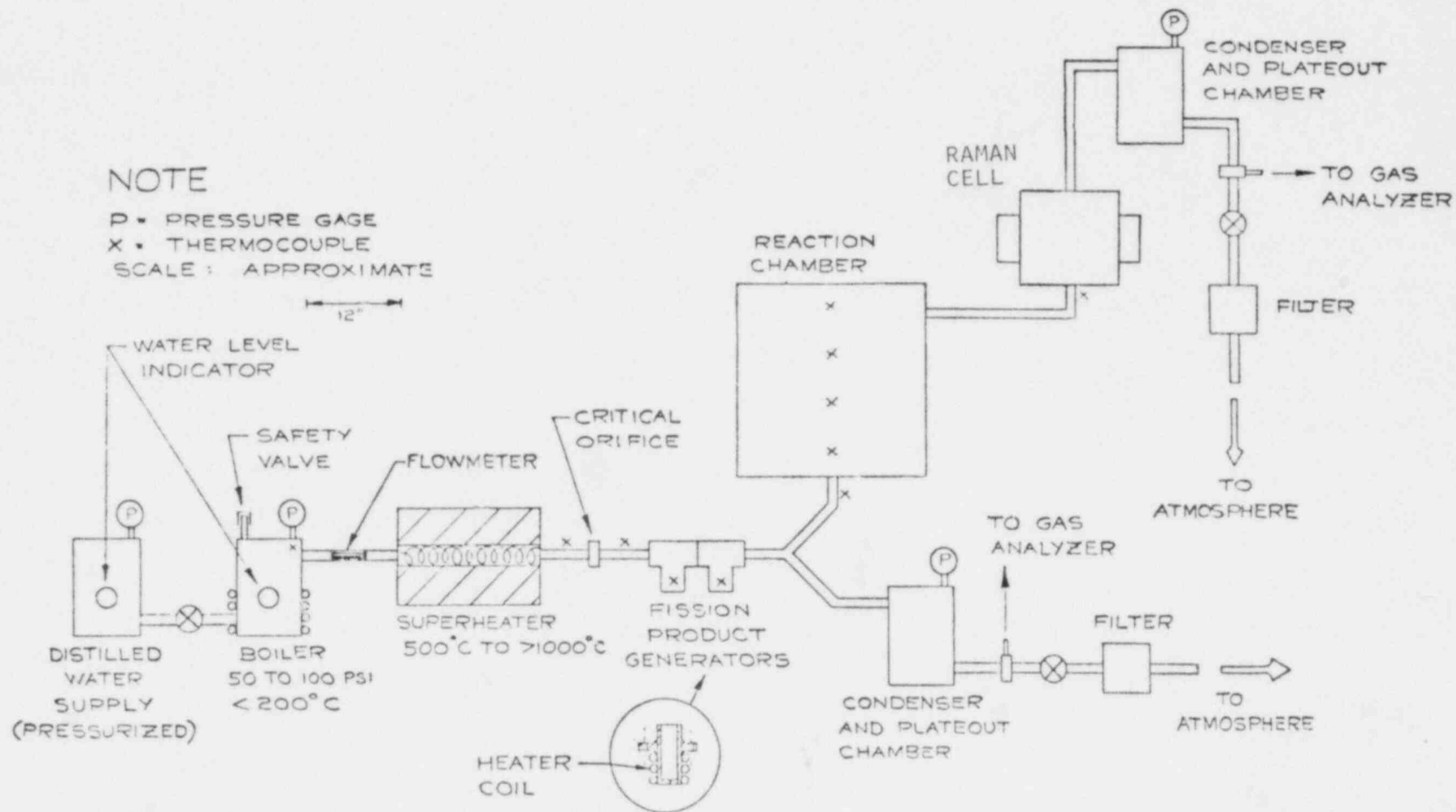


Figure 3-1. Fission Product Reaction Facility

4. Containment Emergency Sump Performance (G. G. Weigand, M. Berman, R. R. Prairie)

4.1 Summary

A loss-of-coolant accident (LOCA) in a pressurized water reactor (PWR) will normally activate the reactor's emergency core cooling system (ECCS). The ECCS supplies coolant to the reactor core to dissipate the decay heat, and under certain conditions, to the containment spray system (CSS) to reduce containment pressure and scrub radioactive material from the containment environment. A failure of the ECCS can be serious; the disruption of core coolant flow could lead to core damage.

The containment emergency sump performance (CESP) program will investigate the reliability of ECCS sumps. The CESP program provides technical direction to the DOE-sponsored experimental sump program at Alden Research Laboratory (ARL), and it has two main purposes:

- to provide a containment-sump data base to NRC, and
- to provide ECCS sump design information to the nuclear industry.

The test program is behind schedule as a result of delays in completing the test facility. ARL has now completed the test facility, component performance checks, and configurations for the check-out tests. ARL projects that the check-out tests

will be completed and initial testing will begin by July 31, 1980. It should be noted that the check-out tests will do more than just confirm the operability of the test facility. We have designed a test series which will check the validity of many of the assumptions which were made when formulating the test plan. This will allow time for redirection of the test plan, should any serious difficulty arise. The initial phase of the test plan is completed; we presented the plan and it was approved at a joint NRC, Sandia, and DOE meeting (May 30, 1980). We also established a time schedule for the adoption of the remaining test program. The schedule calls for final program approval and the forwarding of the test program to ARL for implementation by November 31, 1980.

Sandia has continued with the development of its data reduction planning; the data will be analyzed using analysis of variance, regression analysis and dimensionless empirical correlation. The analysis of variance will be performed using the BIOMED¹ computer program library and a stepwise multiple regression program². The results from the statistical code evaluations plus non-dimensional analysis techniques will be used to perform the empirical data correlations.

4.2 Sump Geometry and Test Variable Definitions

The sump geometry and test variable definitions are discussed in detail in Reference 3; for the readers convenience, Figure 4-1 and Table 4-I briefly describe and define the sump variables.

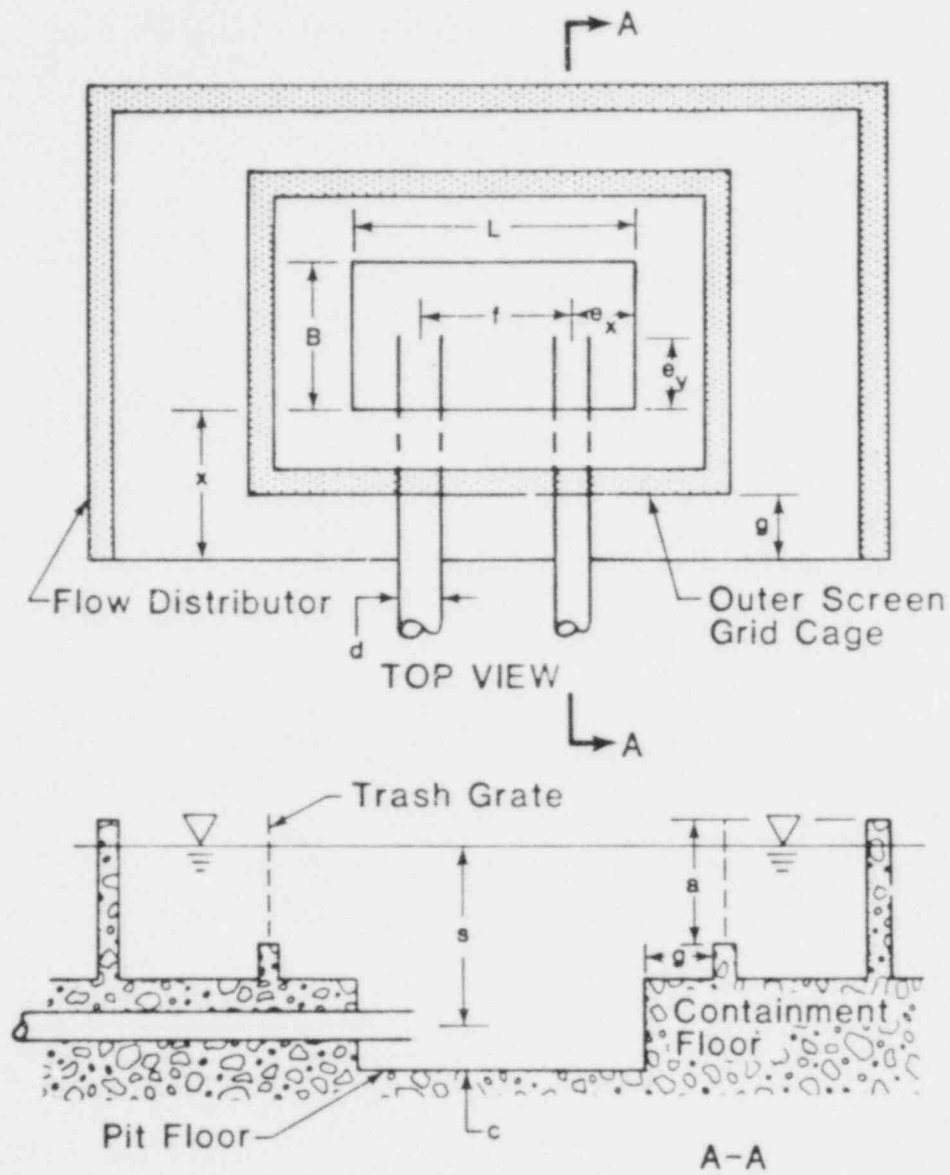


Figure 4-1. Details of the ECCS Sump under Investigation in the CESP Program

TABLE 4-I

Sump Geometric, Flow and Fluid Property Variables

<u>Geometric Variables</u>	<u>Flow Variables</u>	<u>Fluid Property</u>
1. Pipe diameter, d	1. Volumetric Flow per pipe, Q	1. Density, ρ
2. Sump length, L	2. Circulation, Γ	2. Viscosity, μ
3. Sump width, B	3. Submergence, s	3. Surface tension, σ
4. Approach depth at screen, a		
5. Screen distance from sump wall, g		
6. Depth to pipe entrance from building floor, b		Acceleration due to gravity, G
7. Depth to pipe entrance from sump floor, c		
8. Pipe entrance orientation parameters, e_x, e_y		
9. Pipe spacing, f		
10. Wall clearance, x		

4.3. Test Planning

Meetings with NRC, DOE and Sandia representatives during this quarter have resulted in a completed test plan for the first 25 configuration tests; moreover, a time schedule has been agreed upon for arriving at a test plan for the remaining program.

July 31, 1980 -- Sandia delivers a working draft of the test plan to NRC.

Late July, early August -- Sandia, NRC and DOE representatives meet with ARL personnel to solicit their input and to observe the operation of the test facility.

Mid to late September -- Follow-up meeting with NRC and DOE to modify the test plan as a result of information received by NRC from the utilities and from early results of ARL's testing.

November 31, 1980 -- Approval of test plan by NRC and forwarding of the test plan to ARL.

4.3.1 The First Twenty-Five Configurations

The first set of tests that have been agreed upon consists of the sixteen, twelve-inch diameter fractional factorial configurations; sensitivity tests for the e_y variation effects, c variation effects,

non-symmetrical outlet pipes, and cover plate effects; and four reconfigurations for the Task 3 and Task 4 type testing¹. Table 4-II shows the twenty-five configurations under investigation. Note that for several of the configurations in Table 4-II, the complete dimensional specification is not given. These particular configurations involve sensitivity tests, and their exact dimensional specification will be selected by ARL (in consultation with Sandia) using pre-test results. We implemented this procedure so the sensitivity testing would be done in sump configurations where meaningful results will be obtained. In Table 4-II, the specifications X_{19} , X_{23} , and X_{25} are the Task 3 and 4 tests, and will be done on selected configurations; the configurations will be selected on the basis of prior test results. The X_{19} , X_{23} , and X_{25} testing will examine blockage, break flow, condenser drain flow, transients, and non-uniform approach and obstructed flows.

Blockage: ARL will test 8 blockage configurations. They will test six of the proposed worst case blockage configurations in Figure 4-2 and will develop two additional blockage patterns using the sump response as an indicator.

Break Flow: Break flows will be simulated both above and below the water surface using a high speed jet.

Condenser Drain Flow: The condenser drain flows will be simulated with a low speed jet; bubble entrainment is the principle concern.

TABLE 4-II

First Twenty-five Test Configurations

Test No	Config. No	Sump Size (ft x ft)	Configuration Variables								
			d (ft)	b (ft)	e _x (ft)	g (ft)	f (ft)	c (ft)	a (ft)	x (ft)	e _y (ft)
1	57	8x10	1	3	2	1	4	1.5	3	7.5	1
2	15	8x10	1	3	2	1	4	1.5	6	7.5	1
3	13	16x4	1	3	2	1	12	1.5	6	7.5	1
4	11	16x10	1	3	2	1	12	1.5	6	7.5	1
5	12	16x10	1	3	6	3	4	1.5	6	7.5	1
6	9	16x15	1	3	6	1	4	1.5	6	7.5	1
7	8	16x15	1	3	2	3	12	1.5	6	7.5	1
8	5	20x10	1	3	6	1	8	1.5	6	7.5	1
9	4	20x10	1	3	2	3	16	1.5	6	7.5	1
10	1	20x15	1	3	2	1	16	1.5	6	7.5	1
11	2	20x15	1	3	6	3	8	1.5	6	7.5	1
12	43	*	1	3	*	*	*	1.5	6	7.5	3
13	44	*	1	3	*	*	*	1.5	6	7.5	6
14	45	*	1	3	*	*	*	1.5	6	7.5	10
15	49	*	1	3	*	*	*	0.5	6	7.5	1
16	50	*	1	3	*	*	*	2.5	6	7.5	1
17	51	*	1	3	*	*	12	1.5	6	7.5	1
18	52	*	1	3	*	*	8	1.5	6	7.5	1
19	53	*	1	3	*	*	4	1.5	6	7.5	1
X ₁₉ Task 3 and Task 4 testing											
20	16	8x4	1	6	2	1	4	1.5	6	7.5	1
21	14	8x15	1	6	2	1	4	1.5	6	7.5	1
22	7	16x15	1	6	2	1	12	1.5	6	7.5	1
23	3	20x10	1	6	2	1	16	1.5	6	7.5	1
X ₂₃ Task 3 and Task 4 testing											
24	1	16x10	1	10	2	1	12	1.5	6	7.5	1
25	6	20x4	1	10	2	1	16	1.5	6	7.5	1
X ₂₅ Task 3 and Task 4 testing											

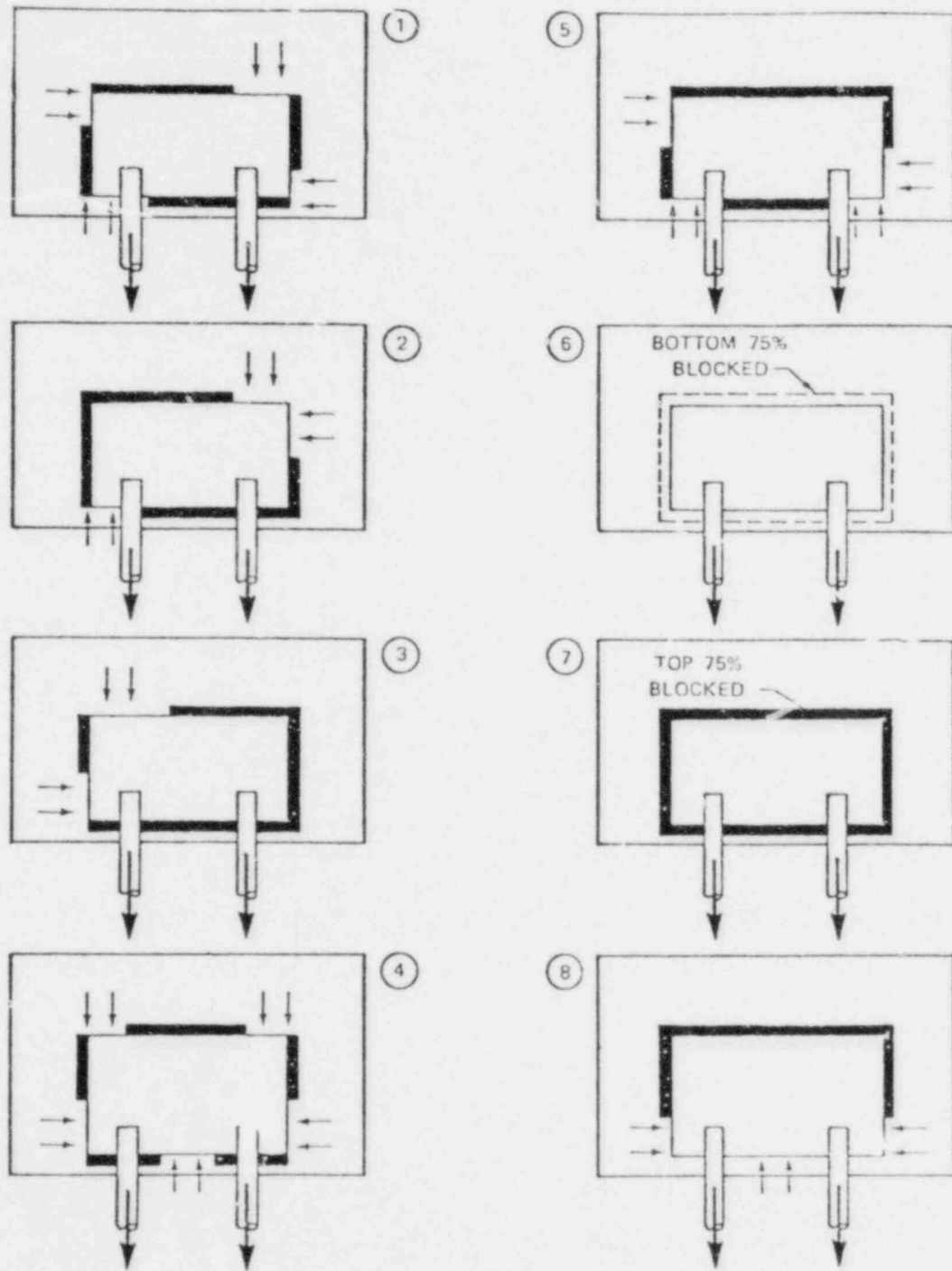


Figure 4-2. Screen Blockage Schemes Suggested for Tests

Transients: The transient which will be simulated is the single outlet operation (loss of one cooling line) versus dual outlet operation (normal operation). Single outlet pipe operation requires a 50% increase in the normal flow per pipe.

Non-Uniform Approach and Obstruction Tests: The non-uniform approach flow tests will study the four flow patterns given in Figure 4-3; these approach patterns represent the worst case approach conditions. Obstruction tests using a cylindrical obstruction will be performed for the same four configurations; the obstruction will be moved about in the approach stream until the worst perturbation is found. The obstruction tests should determine if obstructions such as structural members or pipes could pose serious problems and thus require more investigation.

4.4 Data Analysis

As indicated in the summary, Sandia will analyze the sump data using analysis of variance, regression analysis, and dimensionless empirical correlation. The analysis of variance technique partitions the total variance in the measured variable into independent parts -- each part associated with a factor (measured variable) of the experiment. This information will allow us to estimate factor effects and to perform associated tests of factor significance. Regression analysis provides a systematic method for developing a prediction equation for estimating, with confidence limits, a response surface as a function of the independent factors. The resulting response relation provides an indication of the sensitivity of the response surface to changes in levels of

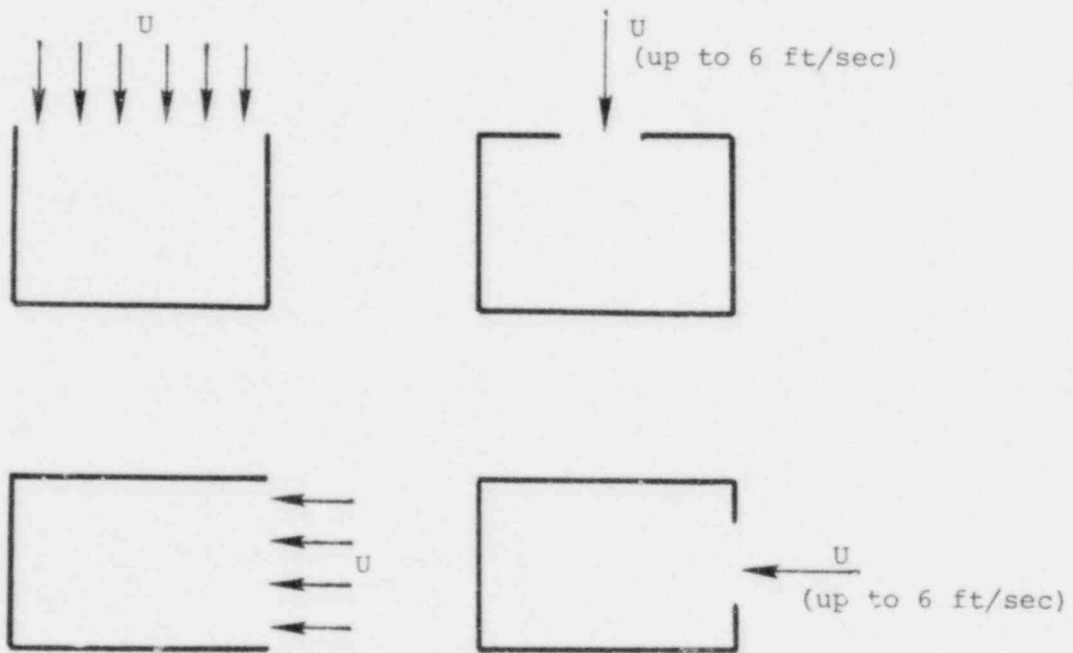


Figure 4-3. Proposed Nonuniform Approach Flow Tests

the independent variables. The dimensionless empirical correlation will use the information gained in performing the analysis of variance and the regression analysis to produce plots, charts, or empirical expressions for the main sump behavior as a function of the main dimensionless numbers. The remainder of this section will address some of the details of statistically analyzing the experiment designs; since the empirical correlation work will be influenced by the statistical results, their development has been deferred until the initial testing is performed.

The main body of the test design consists of two fractional factorials; these two designs were introduced and discussed in Reference 3 and they will be briefly reviewed here. Tables 4-III and 4-IV show the fractional factorial test plans. The -, 0, + designations in each of the tables represent a low, median and high value for each variable range. Table 4-III describes a $(1/3 \times 3^4)$ fractional factorial for the variables d, L, B, and b, whereas Table 4-IV describes a $(1/2 \times 2^5)$ fractional factorial for the variables d, L, B, e_x , and g; the variables flow, Q, and submergence, s, are also included in each of the test designs.

The data from the two fractional factorial experiments will be analyzed separately and in combination. Analysis of variance and regression analysis will be the primary techniques used. The analysis of variance will be performed using the BIOMED¹ code package and the regression analysis

TABLE 4-III

Fractional Factorial Design ($1/3 \times 3^4$)
for the Factors d, L, B, and b

Trial	d	L	B	b	e_x	g
1	0	-	-	-	-	-
2	-	0	-	-	-	-
3	-	-	0	-	-	-
4	-	-	-	0	-	-
5	0	0	0	0	-	-
6	+	0	0	-	-	-
7	0	+	0	-	-	-
8	0	0	+	-	-	-
9	+	0	-	0	-	-
10	0	+	-	0	-	-
11	0	0	-	+	-	-
12	+	-	0	0	-	-
13	0	-	+	0	-	-
14	0	-	0	+	-	-
15	-	+	0	0	-	-
16	-	0	+	0	-	-
17	-	0	0	+	-	-
18	+	+	-	-	-	-
19	+	-	+	-	-	-
20	+	-	-	+	-	-
21	-	+	+	-	-	-
22	-	+	-	+	-	-
23	-	-	+	+	-	-
24	+	+	+	0	-	-
25	+	+	0	+	-	-
26	+	0	+	+	-	-
27	0	+	+	+	-	-

TABLE 4-IV

Fractional Factorial Design ($1/2 \times 2^5$)
for the Factors d, L, B, e_x , and g

<u>Trial</u>	<u>d</u>	<u>L</u>	<u>B</u>	<u>b</u>	<u>e_x</u>	<u>g</u>
1	-	0	0	-	-	-
2	+	+	+	-	+	-
3	+	+	+	-	-	+
4	-	0	0	-	+	+
5	+	+	0	-	+	+
6	-	0	+	-	-	+
7	-	0	+	-	+	-
8	+	+	0	-	-	-
9	+	0	+	-	+	+
10	-	+	0	-	-	+
11	-	+	0	-	+	-
12	+	0	+	-	-	-
13*	-	+	+	-	-	-
14	+	0	0	-	+	-
15	+	0	0	-	-	+
16	-	+	+	-	+	+

*Same as trial 21 in Table III.

will be performed with a Sandia regression code². The regression program performs a stepwise multiple regression; the code is capable of performing stepwise or backward elimination solution and also provides a check on the adequacy of the prediction equation via calculation of the Predicted Error Sum of Squares (PRESS). Additionally this code has the capability of introducing a transformation (rank transform) which will allow a better fit to data which do not have the normal distribution character.

4.4.1 (1/3 x 3⁴) Fractional Factorial Experiment

The form of the analysis of variance is shown in Table 4-V. Tests of significance will be performed on the variables' main effects and their interaction effects by comparing the mean square residual, M_R , with the other mean squares by use of the F statistic.⁴ The mean square residual, defined as

$$M_R = \frac{\sum \{Y_i - \phi(\phi_i)\}^2}{(\text{degrees of freedom})}$$

where

- Y_i data response
- ϕ variance model response
- ϕ independent variables,

TABLE 4-V

Form of Analysis of Variance for Three Level Factors
d, L, B, and b

<u>Source of Variation</u>	<u>Degrees of Freedom</u>	<u>Mean Squares</u>
Pipe diameter (d)	2	M_d
Sump length (L)	2	M_L
Sump width (B)	2	M_B
Pipe depth from floor (b)	2	M_b
d x L	2	M_{dxL}
d x B	2	M_{dxB}
d x b	2	M_{dxb}
L x B	2	M_{LxB}
L x b	2	M_{Lxb}
B x b	2	M_{Bxb}
Residual	6	M_R
TOTAL	26	

is a baseline or norm which all of the other mean squares are compared to for a test of significance. For example, if the ratio M_L/M_R were large when compared with one, then we could conclude that the variable L has a significant main effect. Those effects that are determined to be significant will be displayed graphically and by tables.

Regression analysis will be performed to obtain a prediction between the response variable and the geometric variables d, L, B, and b; moreover, the flow rate, Q, and submergence, s, can also be incorporated as dependent variables in the response surface. This would allow the response surface's goodness of fit to be studied as a function of the order of the Q and s terms in the response equation. We will use the rank transform and PRESS options in the stepwise regression program to determine the best prediction equation. The resulting prediction equation will then be used to develop a response surface; confidence limits will also be given.

4.4.2 (1/2 x 2⁵) Fractional Factorial Experiment

The form of the analysis of variance for the experiment is shown in Table 4-VI. For this experiment we are not initially able to obtain an estimate of the experimental error because we assumed the possibility of many higher order interactions (see Table 4-VI and thus consumed all of the system's degrees of freedom. Thus initially we will use some other method of assessing statistical significance such as half normal plots.⁵ However, if the initial analysis indicates several nonsignificant interaction

TABLE 4-VI

Form of Analysis of Variance for Two Level Factors
d, L, B, e_x , and g

<u>Source of Variation</u>	<u>Degrees of Freedom</u>	<u>Mean Squares</u>
Pipe diameter (d)	1	M_d
Sump length (L)	1	M_L
Sump width (B)	1	M_B
Orientat'on parameter (e_x)	1	M_{e_x}
Pipe depth from floor (b)	1	M_b
d x L	1	M_{dxL}
d x B	1	M_{dxB}
d x e_x	1	M_{dxe_x}
d x b	1	M_{dxb}
L x B	1	M_{LxB}
L x e_x	1	M_{Lxe_x}
L x b	1	M_{Lxb}
B x e_x	1	M_{Bxe_x}
B x b	1	M_{Bxb}
e_x x b	1	M_{e_xxb}
TOTAL	16	

effects, then they can be pooled together to obtain an estimate of the experimental error. Appropriate tables and graphs will be constructed.

4.4.3 Combined Fractional Factorial Results.

In addition to analyzing each of the fractional factorial experiments individually, we will combine the data and perform a single regression analysis; once again the variables Q and s will be incorporated into the response surface. The main objective will be to determine the important independent variables, the sensitivity of the response to the important independent variables, and the best prediction equation. The prediction equation will be used to develop a response surface with appropriately defined confidence limits.

4.5 References

- ¹W. J. Dixon, Ed., BMDP Biomedical Computer Programs, P-series 1977, School of Medicine, University of California, Los Angeles, University of California Press, Los Angeles, California, 1977.
- ²R. L. Iman, et al., Stepwise Regression with PRESS and Rank Regression (Program Users Guide), SAND79-1472, Sandia National Laboratories, Albuquerque, New Mexico, January 1980.
- ³G. G. Weigand, M. Berman, R. R. Prairie, "Containment Emergency Sump Performance," Light Water Reactor Safety Research Program Quarterly Report January - March 1980, SAND80-1301/1of4, NUREG/CR-1509/1of4, M. Berman, Person in Charge, Sandia National Laboratories, Albuquerque, New Mexico, July 1980.
- ⁴A. Hald, Statistical Theory with Engineering Applications, John Wiley & Sons, Inc., 1952.
- ⁵C. Daniel, "Use of Half-Normal Plots in Interpreting Factorial Two-Level Experiments," Technometrics, Vol. 1, 1959, pp. 311-341.

DISTRIBUTION:

US Nuclear Regulatory Commission (400 copies for R3)
Division of Document Control
Distribution Services Branch
7920 Norfolk Avenue
Bethesda, MD 20014

US Nuclear Regulatory Commission (7)
Office of Nuclear Regulatory Research
Washington, DC 20555
Attn: R. DiSalvo
S. Fabric
D. A. Hoatson
C. E. Johnson
R. R. Sherry
C. Z. Serpan
L. H. Sullivan

US Nuclear Regulatory Commission (6)
Division of Systems Safety
Office of Nuclear Reactor Regulation
Washington, DC 20555
Attn: T. P. Speis
J. F. Meyer
N. Lauben
J. K. Long
A. R. Marchese
W. R. Butler

US Department of Energy
Operational Safety Division
Albuquerque Operations Office
P. O. Box 5400
Albuquerque, NM 87185
Attn: J. R. Roeder, Director

Kraftwerk Union (2)
Hammerbacher strasse 12 & 14
Postfach 3220
D-8520 Erlangen 2
Federal Republic of Germany
Attn: Dr. M. Peehs
Dr. K. Hassmann

Gesellschaft für Kern Forschung (2)
75 Karlsruhe
Postfach 3640
Federal Republic of Germany
Attn: Dr. J. P. Hosemann
Dr. S. Hagen

Dr. H. Karwat
Technische Universitaet Muenchen
D-8046 Garching
Federal Republic of Germany

Distribution (cont'd):

Prof. F. Mayinger
Technische Universitaet Hannover
3000 Hannover 1
Federal Republic of Germany

Dr. M. V. Banaschik
Gesellschaft Fuer Reakforsicherheit (GRS)
Postfach 101650
Glockengasse 2
5000 Koeln 1
Federal Republic of Germany

Swedish State Power Board (2)
El-Och Vaermeteknik
Sweden
Attn: Eric Ahlstroem
Wiktors Frid

M. El-Genk
EG&G - Idaho, Inc.
P. O. Box 1625
Idaho Falls, ID 83401

R. A. Bari
Brookhaven National Laboratory
Upton, NY 11973

M. L. Stevenson
Los Alamos Scientific Laboratory
P. O. Box 1663
Los Alamos, NM 87545

Electric Power Research Institute (2)
3412 Hillview Avenue
Palo Alto, CA 94303
Attn: J. Carey
L. B. Thompson

D. H. Walker
Offshore Power System
8000 Arlington Expressway
Box 8000
Jacksonville, FL 32211

L. Hochreiter
Westinghouse Corp.
Nuclear Energy Systems
P. O. Box 350
Pittsburgh, PA 15230

Prof. S. Abdul-Kalik
Nuclear Engineering Department
University of Wisconsin
Madison, WI 53706

Distribution (cont'd):

S. G. Bankoff
Chemical Engineering Department
Northwestern University
Evanston, IL 60201

1223 R. R. Prairie
2510 D. H. Anderson
2513 J. E. Kennedy
2514 D. E. Mitchell
4000 A. Narath
4400 A. W. Snyder
4410 D. J. McCloskey
4412 J. W. Hickman
4414 G. B. Varnado
4414 A. S. Benjamin
4414 W. B. Murfin
4420 J. V. Walker
4421 R. L. Coats
4422 D. A. Powers
4422 R. M. Elrick
4424 W. Breitung
4425 W. J. Camp
4440 G. R. Otey
4441 M. Berman (15)
4441 R. K. Cole, Jr.
4441 M. L. Corradini
4441 J. C. Cummings
4441 J. F. Muir
4441 M. P. Sherman
4441 G. G. Weigand
4442 W. A. Von Rieseemann
4443 D. A. Dahlgren
4444 S. L. Thompson
4444 L. D. Buxton
4444 R. K. Byers
4445 L. O. Cropp
4450 J. A. Reuscher
5130 G. A. Samara
5131 B. Morosin
5131 W. B. Benedick
5512 D. W. Larson
5520 T. B. Lane
5521 L. W. Davison
5530 W. Herrmann
5534 J. F. Assay
5534 D. S. Drumheller
5830 M. J. Davis
5836 J. L. Ledman
5836 L. S. Nelson
5846 E. K. Beauchamp
5846 R. A. Sallach
8266 E. A. Aas
3141 T. L. Werner (5)
3151 W. L. Garner (3)
For DOE/TIC (Unlimited Release)
3154-3 R. P. Campbell (25)
For NRC Distribution to NTIS